12-2015

Numerical Study of Synthetic-Jet Actuation Effect on Airfoil Trailing Edge Noise

Marco Sansone

Numerical Study of Synthetic-Jet Actuation Effect on Airfoil Trailing Edge Noise

A Thesis

Submitted to the Faculty

of

Embry-Riddle Aeronautical University

by

Marco Sansone

In Partial Fulfillment of the

Requirements for the Degree

of

Master of Science in Aerospace Engineering

December 2015

Embry-Riddle Aeronautical University

Daytona Beach, Florida

Numerical Study of Synthetic-Jet Actuation Effect on
Airfoil Trailing Edge Noise

by

Marco Sansone

A Thesis prepared under the direction of the candidate's committee chairman, Dr. Vladimir Golubev, Department of Aerospace Engineering, and has been approved by the members of the thesis committee. It was submitted to the School of Graduate Studies and Research and was accepted in partial fulfillment of the requirements for the degree of Master of Science in Aerospace Engineering.

THESIS COMMITTEE

Vladimir Golubev
Digitally signed by Vladimir Golubev
Date: 2015.12.02 11:24:24 -05'00'

Chairman, Dr. Vladimir Golubev

Reda Mankbadi
Digitally signed by Reda Mankbadi
Date: 2015.12.02 12:21:55 -05'00'

Member, Dr. Reda Mankbadi

PASILIAO.CRYSTAL.L.1265299772
Digitally signed by PASILIAO.CRYSTAL.L.1265299772
DN: c=US, o=U.S. Government, ou=DoD, ou=PKI, ou=USAF, cn=PASILIAO.CRYSTAL.L.1265299772
Date: 2015.12.02 13:37:02 -06'00'

Member, Dr. Crystal Pasiliao

Anastasios (Tasos) Lyrintzis
Digitally signed by Anastasios (Tasos) Lyrintzis
Date: 2015.12.02 15:02:53 -05'00'

Member, Dr. Anastasios Lyrintzis

REASOR.DANIEL.ARCHER.JR.1366851867
Digitally signed by REASOR.DANIEL.ARCHER.JR.1366851867
DN: c=US, o=U.S. Government, ou=DoD, ou=PKI, ou=USAF, cn=REASOR.DANIEL.ARCHER.JR.1366851867
Date: 2015.12.02 14:20:35 -06'00'

Member, Dr. Daniel Reasor

Anastasios (Tasos) Lyrintzis
Digitally signed by Anastasios (Tasos) Lyrintzis
Date: 2015.12.02 15:02:32 -05'00'

Department Chair, Dr. Anastasios Lyrintzis
or Graduate Program Coordinator, Dr. Eric Perrell

12/02/2015
Date

Maj Mirmirani
Digitally signed by Maj Mirmirani
DN: cn=Maj Mirmirani, o=Embry-Riddle Aeronautical University, ou=College of Engineering, email=mirmiram@erau.edu, c=US
Date: 2015.12.02 16:53:29 -05'00'

Dean of College of Engineering, Dr. Maj Mirmirani

12/02/2015
Date

Christopher Grant
Digitally signed by Christopher Grant
DN: cn=Christopher Grant, o=ERAU, ou=College of Engineering, email=grantch@erau.edu, c=US
Date: 2015.12.03 12:20:48 -05'00'

Associate VP for Academics, Dr. Christopher Grant

12/02/2015
Date

ACKNOWLEDGMENTS

I would like to acknowledge my research teammates Lap Nguyen and Sam Salehian for all the help and support they've given that has gone towards the completion of this thesis. I'd also like to thank my advisors Dr. Vladimir Golubev and Dr. Reda Mankbadi for their guidance and the opportunity to work on this project as well as the patronage of the AFRL program and my Air Force advisors Dr. Crystal Pasiliao and Dr. Daniel Reasor who helped expand the study.

TABLE OF CONTENTS

LIST OF TABLES

LIST OF FIGURES

SYMBOLS

v_m	Amplitude of SJA actuation
A	Area of SJA orifice
c	Chord length
C_d	Coefficient of Drag
C_f	Coefficient of friction
C_L	Coefficient of Lift
C_p	Coefficient of Pressure
dB	Decibels
S	Depth of SJA Orifice
v_{SJA}	Exit Velocity for SJA
C_{Lfft}	Fast Fourier Transform of Lift
P_{fft}	Fast Fourier Transform of pressure signal
γ	Heat capacity ratio
ω_a	Non-dimensional Actuation Frequency
ω	Non-dimensional Frequency
τ	Non-dimensional time TAU
P_{RMS}	Root mean square of pressure signal
ξ	Transformed x
η	Transformed y
ζ	Transformed z
ρ_∞	Upstream Density
M_∞	Upstream Mach number
T_∞	Upstream Temperature
u_∞	Upstream Velocity

ABBREVIATIONS

AoA	Angle of Attack
CAA	Computational Aero-Acoustics
DNS	Direct Numerical Simulation
Hz	Hertz
ILES	Implicit Large Eddy Simulations
KH	Kelvin-Helmholtz waves
KE	Kinetic Energy
LES	Large Eddy Simulations
LDA	Laser-Doppler Anemometry
Pr	Prandtl number
RANS	Reynolds-Averaged Navier–Stokes
Re	Reynolds number
SJA	Synthetic-Jet Actuator
TS	Tollmien-Schlichting waves
UAV	Unmanned Aerial Vehicle

ABSTRACT

Sansone, Marco MSAE, Embry-Riddle Aeronautical University, December 2015.

Numerical Study of Synthetic-Jet Actuation Effect on Airfoil Trailing Edge Noise.

The current study conducts numerical simulations to assess the possibility of employing Synthetic-Jet Actuators (SJAs) as active noise control devices for reduction of airfoil acoustic radiation. High-accuracy numerical efforts employ a sixth-order accurate Navier–Stokes solver implementing a low-pass filtering of poorly resolved high-frequency solution content to retain numerical accuracy and stability over the range of transitional flow regimes. In the adopted numerical procedure, the actuator is modeled without its resonator cavity through imposing a simple fluctuating-velocity boundary condition at the bottom orifice of the actuator. The orifice cavity with the properly defined boundary condition is embedded into the airfoil surface for conducting high-accuracy viscous analysis of SJA-based active noise control. The effects of SJA location and actuation frequency on airfoil sound radiation are examined for uniform upstream flow conditions.

1. Introduction

1.1. Airfoil Noise

It is well known that the noise produced by an isolated airfoil is highly dependent on the flow regime (Arbey & Bataille, 1983). In the absence of upstream flow non-uniformities, the dominant mechanism of trailing-edge noise radiation at high-Re is related to the acoustic scattering of the airfoil turbulent boundary layer convecting at the airfoil's trailing edge (Ewert & Manoha, 2007). The acoustic radiation process involves transforming the quadrupolar (acoustically inefficient) nature of convected eddies into much more acoustically efficient dipolar sources still producing generally moderate noise levels. On the other hand, as recently reviewed in the work by (Golubev et al., 2014), a low-speed airfoil with transitional boundary layer may exhibit distinct, highly pronounced tones characteristic of flow-acoustic resonance phenomena associated with feedback-loop interactions between upstream-propagating acoustic waves scattered from the airfoil trailing edge and the rapidly-amplifying boundary-layer instability modes. These tones can be up to $40dB$ higher than the broadband levels of the airfoil.

The exact nature of the noise generation mechanism has had a long history of debate, with many proposed explanations for the generation of tonal noise on transitional airfoils with sharp trailing edges. (Patterson, 1973) noted that the noise resembled the discrete-frequency vortex shedding associated with bluff bodies and proposed that a similar process was responsible for the observations of the airfoils. He formulated a scaling law based on a Strouhal number of 0.2, associated with bluff body shedding, referenced to twice the boundary layer thickness at the trailing edge. (Tam, 1974) disagreed with Patterson's explanation, pointing out that the vortex shedding explanation

was inadequate to explain the observations. Tam proposed the existence of an aerodynamic feedback loop that was revisited by (Golubev et al., 2014) as mentioned earlier. This is illustrated in Figure 1.1, in which disturbances originating at the sharp trailing edge travel downstream and induce lateral oscillations in the wake. Upon reaching a large enough magnitude, acoustic radiation is emitted and travels upstream, forcing the pressure side boundary layer to oscillate, thus completing the feedback loop.

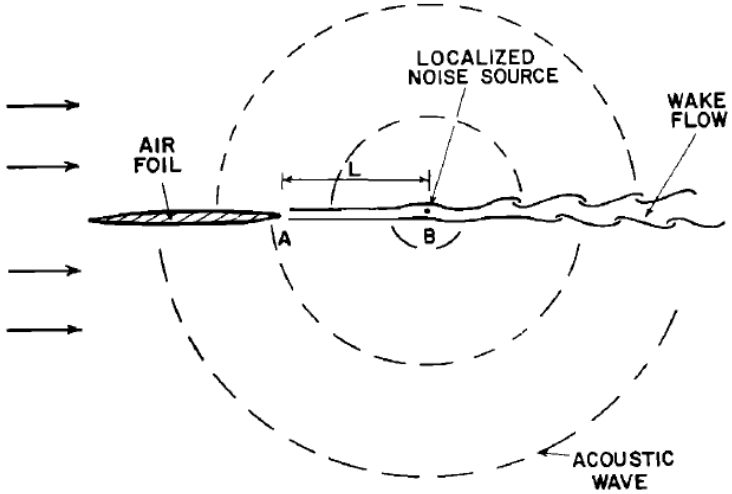

Figure 1.1. Feedback Model Proposed By (Tam, 1974).

(Arbey and Bataille, 1983) proposed another explanation by observing that there was significant similarity between broadband sound in the far-field with wall pressure spectrum near the trailing edge, which exhibited the same peak frequency. Their conclusion was that the broadband noise contribution was due to the growth of instabilities in the boundary layer and their diffraction as acoustic waves at the trailing edge, similar to the generation of noise in a turbulent boundary layer. They also proposed that instability formation began at the maximum velocity point on the airfoil surface due to the beginning of the adverse pressure gradient in this region. In this model, shown in

Figure 1.2, a mode becomes highly amplified if the acoustic waves from the trailing edge are in phase with the disturbances of the same frequency at the maximum velocity point.

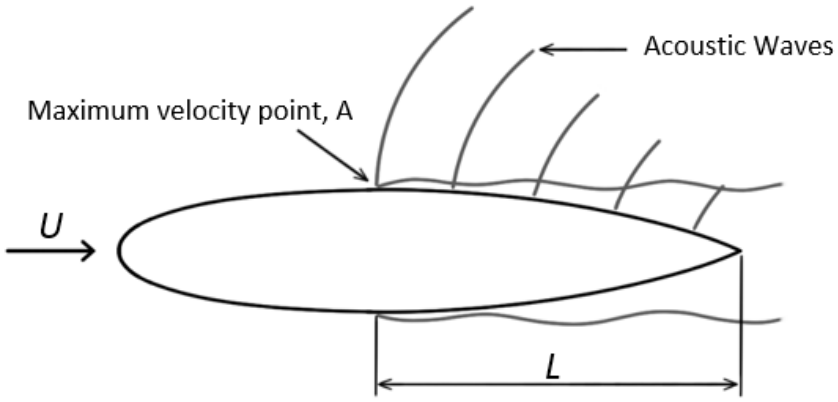

Figure 1.2. Feedback Model Proposed By (Arbey & Bataille, 1983).

Using advanced laser-Doppler anemometry (LDA) techniques, (Nash et al., 1999) found that the adverse pressure gradient on the pressure side leads to the development of inflectional boundary velocity profiles that develop into a region of separated flow near the trailing edge. As shown in Figure 1.3, an instability propagating downstream becomes massively amplified in this region and rolls up into a vortex. These vortices interact with the trailing edge to form a scattered oscillating field around the airfoil with the same frequency as the most amplified instability. They proposed that this oscillating field provides the feedback mechanism to select the most amplified instability, and thus the observed discrete tone.

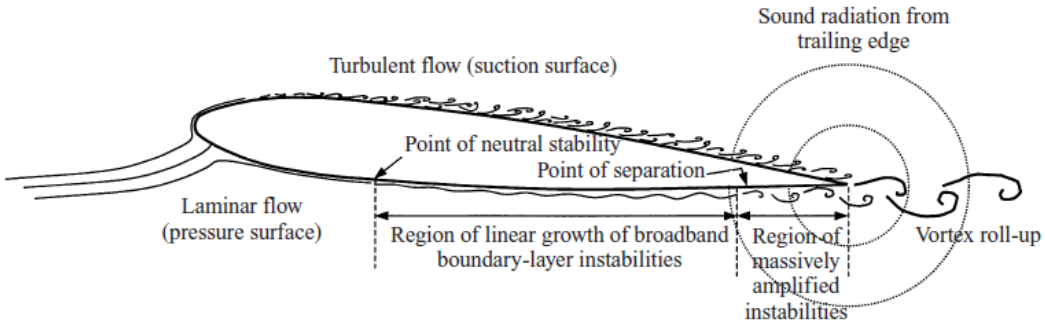

Figure 1.3. Feedback Model Proposed By (Nash et al., 1999).

(Desquesnes et al., 2007) extended the work of (Nash et al., 1999) further by performing 2D direct numerical simulation (DNS) in order to explore the structure and role of flow on the suction surface, which had previously been neglected. Typically the suction surface will refer to the upper surface of a positive lift airfoil. They found that, as in the separation region shown on the pressure side by (Nash et al., 1999) when tones are present a point exists on the suction surface that is near separation which is conducive to the growth of instabilities. They showed by linear stability analysis that while the predicted most-amplified frequency on the pressure surface does correspond very closely with observed tone, there also exist highly amplified frequencies on the suction side as well a slightly different peak frequency. Therefore, it was proposed that an interaction between separate feedback loops on the upper and lower surfaces may have a role in the existence of multiple tones. The model proposed by (Desquesnes et al., 2007) shown in Figure 1.4. It is very similar to that proposed by (Nash et al., 1999), but includes a secondary loop that involves the amplification of Tollmien-Schlichting (TS) waves on the suction surface of the airfoil. These TS waves then transform into Kelvin-Helmholtz (KH) waves that produce vortex structures that are shed at the trailing edge.

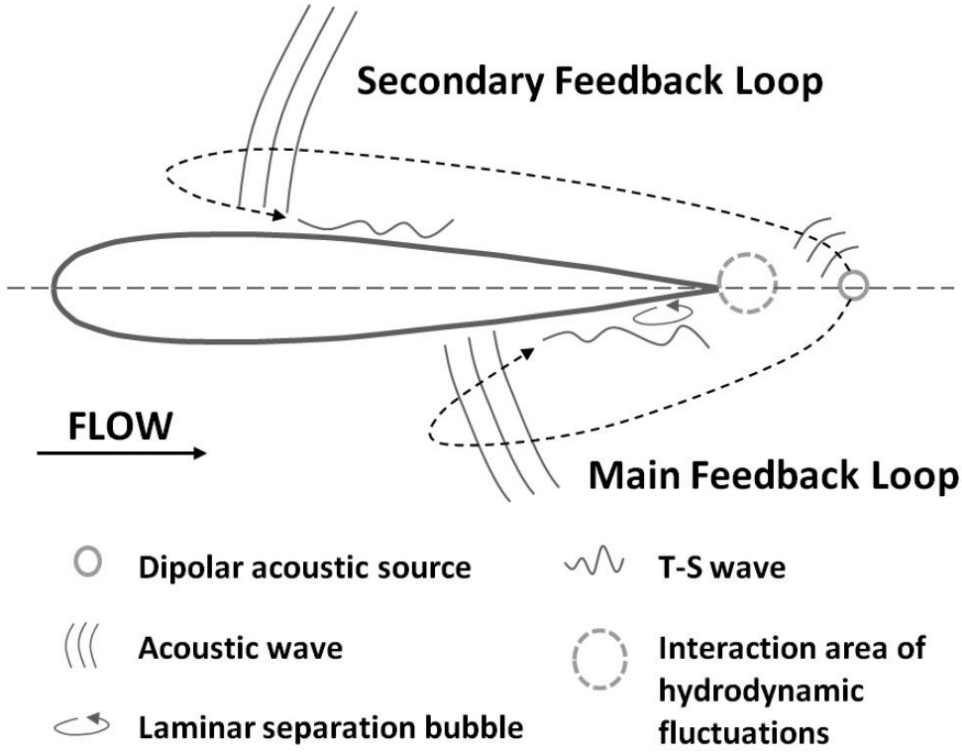

Figure 1.4. Feedback Model Proposed By (Desquesnes et al., 2007).

1.2. Motivation

The implementation of noise control methods on an airfoil can be beneficial for the designs of both military and civilian aircraft. The growing popularity of small unmanned aircraft, UAVs, is of particular interest. The use of UAVs as a means of surveillance or reconnaissance demands that the craft be designed with stealth in mind. As these drones are typically small in size, it is more likely for an enemy combatant to detect the craft by sound than by sight alone, therefore the reduction of a UAVs sound signature decreases the likelihood of it being discovered. In the civilian sector, the use of UAVs is small but growing. Although UAV operation in public airspace is currently restricted, that is expected to change in the coming decade (Callicoat et al., 2013). Within the next ten years, it is likely that UAVs will be flying overhead performing functions

such as traffic monitoring, aerial surveying, and agricultural functions such as crop inspection and crop dusting. Thus, although UAVs have typically been designed without regard to noise considerations, it is becoming of interest to create quiet UAVs.

1.3. Project History

The use of Synthetic-Jet Actuators (SJAs) as an active noise control device was first researched by (Sewell, 2012) and later elaborated in (Mankbadi et al., 2014; Golubev et al., 2015) for a Joukowski airfoil. An SJA is a small device that can be implanted onto an airfoil to inject energy into the flow and is described in the schematic shown in Figure 1.5 (Glezer, Ari & Amitay, 2002). It adds only about a gram to the weight of an airfoil and only requires a small charge to actuate. The main constraint is the cavity size which can take up a sizeable amount of space, especially if embedded near the trailing edge. Contaminants such as dirt or moisture can also impede the effectiveness of the SJA should they enter the cavity. The current study follows the approach developed by (Golubev & Nakhla, 2012) to investigate the effect of an SJA on airfoil flow control using high-fidelity analysis. The Joukowski airfoil and the flow regime were originally chosen to compare with a Computational Aero-Acoustic (CAA) benchmark case for inviscid gust-airfoil interaction (Scott, 2004). Figure 1.6 shows the initial validation results from (Sewell, 2012) specifically the mean pressure over the chord matching the inviscid benchmark until midchord. At this point, separation occurs and viscous effects begin to dominate the flow over the airfoil. This point was chosen as a probable optimal location for the SJA, but the effect of SJA location was not investigated until the current study.

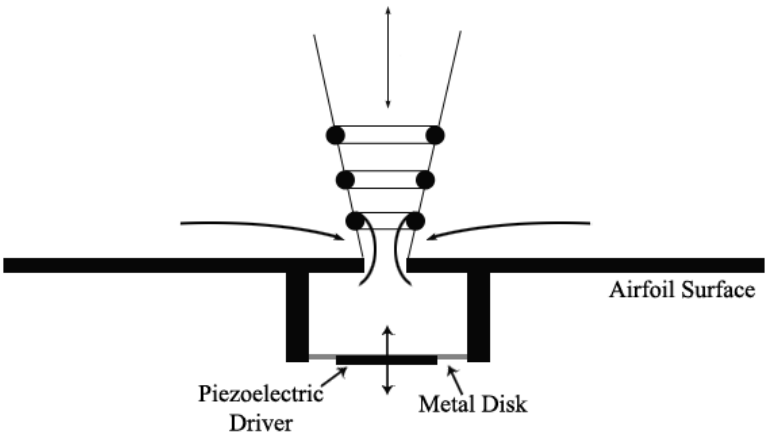

Figure 1.5. Schematic Of A Synthetic-Jet Actuator.

The primary results detailed in (Sewell, 2012) suggested that SJA actuation could reduce tonal noise generation at the trailing edge. It was further suggested that the transitional switching of the separation bubble accounts for most of the sound production and its dampening by the cavity and further dampening by actuation is what reduces the overall acoustic directivities. This separation bubble is shown by the spin of the flow represented by *z*-vorticity in Figure 1.7 The noise dampening is reflected by the directivity plot in Figure 1.8 which shows a reduction in noise levels with the addition of the non-actuating cavity indicated by the drop in pressure levels, and further reduction with the addition of actuation. However, this was a low fidelity analysis with a small acoustic sampling size and a coarse grid. In (Mankbadi, 2014; Golubev, 2015), grid validation was performed and a finer mesh was chosen to better resolve the acoustic nearfield. Noise reduction was seen again with the use of SJAs, but it was also determined that SJAs had no effect under upstream gust conditions. The new data along with the finer mesh suggested that the geometry change present with the addition of a non-actuating cavity did not have a significant effect on the flow, contrary to the results of (Sewell, 2012).

1.4. Goals of Current Study

The current study expands on the earlier work by (Sewell, 2012; Mankbadi et al, 2014; Golubev et al., 2015) and numerically investigates the effectiveness of synthetic-jet actuation for active control of airfoil aeroacoustic response for the same high speed Joukowski airfoil regime, with the SJA embedded at midchord. A larger number of frequencies are tested in order to evaluate their effect on noise suppression. Trends are examined as part of a preliminary optimization study to help choose future starting frequency parameters. Furthermore, preliminary SJA location optimization is investigated by comparing the noise suppression of the SJA placed at midchord with that of an SJA placed at 90% chord.

The robustness of the method was investigated with the inclusion of an alternate airfoil in a different regime. Preliminary data from a separate ongoing study investigating a low speed, high-Re transitional NACA 0012 airfoil was used as a starting point. The 0°AoA case was predicted to not have separation at midchord, so higher AoAs were tested in an attempt to bring the separation point to the midchord SJA location to match the conditions of the Joukowski cases. The SJA was placed once again at midchord, and comparisons were made between cases with and without actuation for each AoA.

Finally, frequency resolution for all cases was increased thanks to improved post processing scripts. The original study by (Sewell, 2012) was restricted to 512 samples over 50 cycles. With the improved scripts it became possible to use 16384 samples over 65 cycles. This improved the spectral resolution from a base frequency of 38Hz to 27Hz, and allowed for better capturing of lower frequencies because of the longer duration. This is in addition to the finer grid validated in (Golubev et al., 2015) that allows for better

capturing of high frequencies.

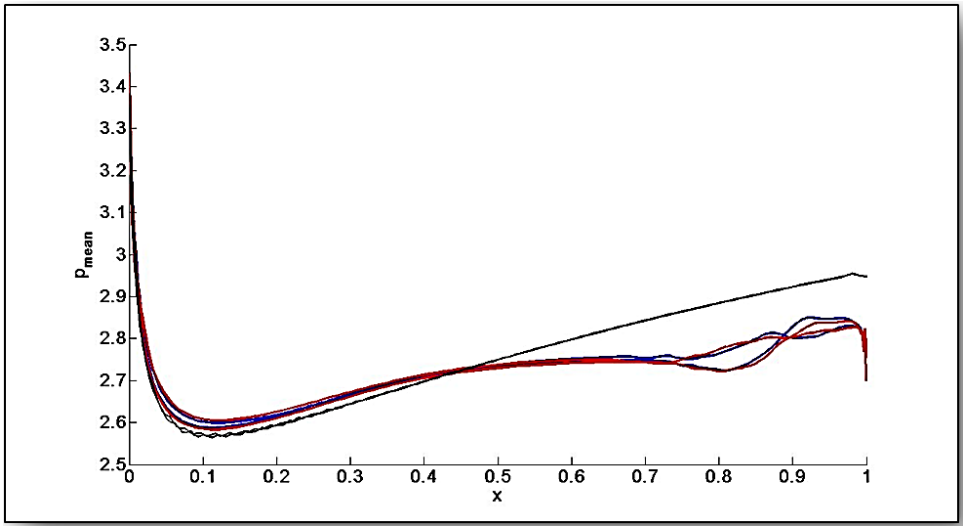

Figure 1.6. Mean Surface Pressure On Joukowski With Upstream Gust (Sewell, 2012). Coarse Mesh (Red) Fine Mesh (Blue) Inviscid (Black).

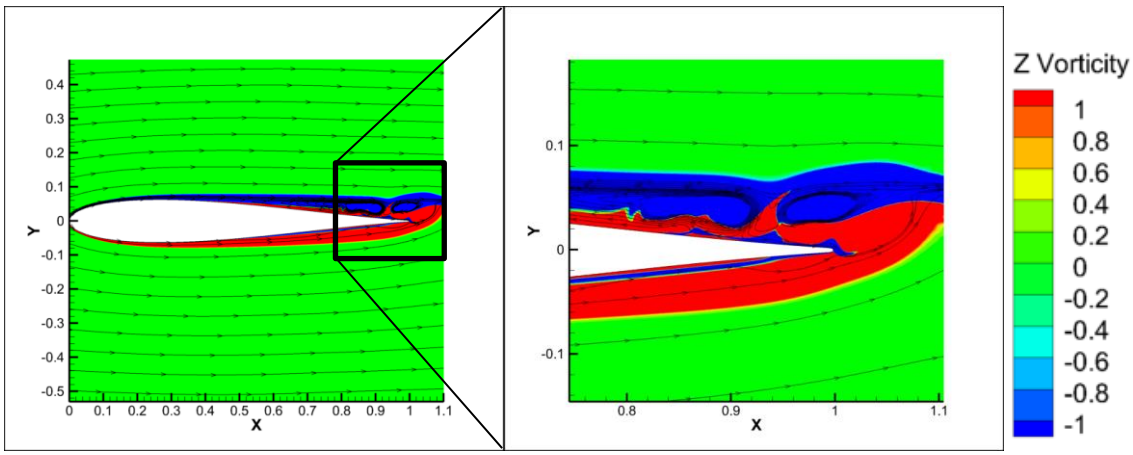

Figure 1.7. z-Vorticity Contours Showing Separation Bubble For Joukowski Airfoil.

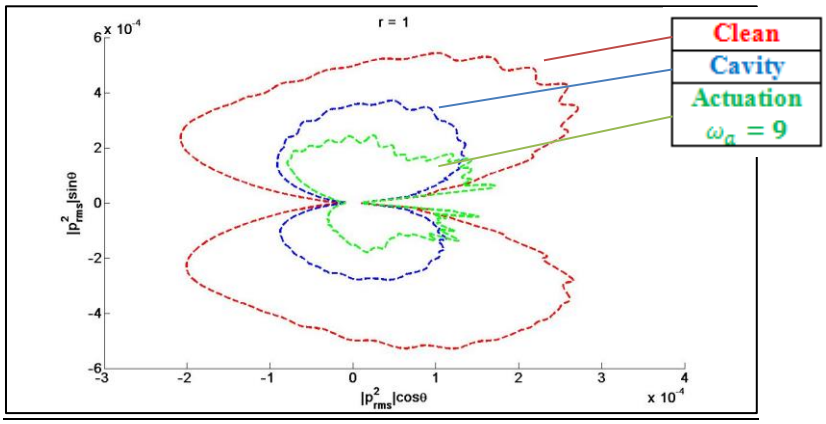

Figure 1.8. Acoustic Directivities At Radius $1c$ (Sewell, 2012). Clean (Red) Cavity (Blue) Actuation (Green).

1.5. Procedure Overview

The effects of synthetic-jet actuation are considered in application to unsteady flow over airfoils and analyzed using a high-accuracy compressible viscous ILES solver (Visbal & Gaitonde, 2002). FDL3DI (2015 version), is the updated solver used in our previous gust-airfoil and vortex-airfoil interaction studies (Golubev, Nguyen, & Visbal, 2010a; Golubev, & Visbal, 2012). In the numerical procedure, all variables are non-dimensionalized by the airfoil chord c and freestream flow density ρ_∞ and flow velocity u_∞. In particular, time and actuation frequency are scaled with both chord length and upstream velocity.

$$t = \tau c/u_\infty,\ f = \omega_a 2\pi c/u_\infty$$

The employed numerical approach was previously tested against various benchmarks (Visbal, M.R. and Gaitonde, D.V., 2002) and was successfully employed in flow control predictions, e.g., by (Rizzetta et al., 1999). The current version of the code employs the developed and successfully tested capability for the high-fidelity analysis of unsteady flow-structure interactions including accurate descriptions of upstream unsteady vortical flow fields used in the current study. The 2D simplification was previously validated against 3D simulations (Golubev et al., 2011).

The ILES solver was chosen as a middle ground between high accuracy DNS solvers that come with much higher runtime requirements, and lower accuracy RANS solvers that cannot effectively capture the acoustic field. A DNS solver would attempt to resolve all of the spatial and temporal scales present in the flow but would require a much finer grid density and very long runtimes. DNS solvers can take months to complete a case, which is not feasible for our purposes. On the other hand, RANS solvers can

complete runs very quickly but as they implement averaging of the Reynolds stresses they dampen the acoustic field. LES solvers use the unaltered Navier–Stokes Equations like DNS to resolve most of the spatial and temporal scales, but use filtering or modelling at the lowest scales. The result is a very accurate solution that can resolve the acoustic field, and can be completed in a few hours when run on parallel CPU nodes. Hybrid RANS-LES solvers exist that switch between models for different parts of the flow, but they can be difficult to implement and unfavorable for complex flows.

Calculations were performed using the Air Force Research Lab's High Performance Computing clusters Lightning (2.7 GHz core speed) and Spirit (2.7 GHz core speed). Two different regimes were tested, as described in the previous section. For each case, the mesh is partitioned into 700 overlapped blocks assigned to different processors to be solved in parallel. The total runtime approaches 10 hours of clock time, or 7,000 CPU hours. Additional wait time must be considered as typically submitted cases on the clusters will wait in queue for a few days.

The code outfiles that are created are used to extract pertinent information using an in-house serial script named CIRCE. The script stores pertinent variables in one condensed file for future post-processing. At the same time, outfiles are converted into a "fast plot3d" format, viewable by Tecplot for use in flow visualization. This process typically lasts around 8 hours. Variables such as P_{RMS} and P_{fft} are then quickly calculated with a number of smaller in-house scripts.

2. Numerical Experiment Setup

The following features of the employed numerical procedure appear particularly beneficial for the current application and further explained in the following sections:

- Implicit time marching algorithms (up to fourth-order accurate) are suitable for the low-Re wall-bounded flows.
- High-order spatial accuracy (up to sixth-order accurate) is achieved by use of implicit compact finite-difference schemes, thus making LES resolution attainable with minimum computational expense.
- Robustness is achieved through a low-pass Pade-type non-dispersive spatial filter (Visbal & Gaitonde, 2002) that regularizes the solution in flow regions where the computational mesh is not sufficient to fully resolve the smallest scales. Note that the governing Navier–Stokes Equations are represented in the original unfiltered form, used unchanged in laminar, transitional, or fully turbulent regions of the flow. The resulting Implicit LES (ILES) procedure employs the high-order filter operator in lieu of the standard subgrid-scale model and heat flux terms. The resulting filter thus selectively damps the evolving poorly resolved high-frequency content of the solution.
- Although the filter is applied explicitly, (Visbal & Gaitonde, 2002) chose to refer to it as a form of ILES due to the fact that in most computations and non-uniform meshes, the filtering step is typically required in order to retain numerical stability even for laminar flows in which transfer of energy to high-frequency is entirely of a numerically spurious nature.
- Overset grid technique is adopted for geometrically complex configurations, with

the high-order interpolation maintaining spatial accuracy at overlapping mesh interfaces.

In the numerical procedure, all variables are non-dimensionalized by the airfoil chord c and freestream flow density ρ_∞ and flow velocity u_∞. The employed numerical approach was previously tested against various benchmarks (Visbal & Gaitonde, 2002) and was successfully employed in flow control predictions, e.g., by (Rizzetta et al., 1999). The current version of the code employs the developed and successfully tested capability for the high-fidelity analysis of unsteady flow-structure interactions including accurate descriptions of upstream unsteady vortical flow fields used in the current study. The 2D simplification was previously validated against 3D simulations (Golubev et al., 2011).

2.1. Governing Equations

The subsonic FDL3DI code solves the conservative, time-dependent form of the Navier–Stokes Equations in generalized curvilinear coordinates (ξ, η, ζ, τ) transformed from the physical coordinates(x, y, z, t).

$$\frac{\delta}{\delta\tau}\left(\frac{\vec{Q}}{J}\right) + \frac{\delta\vec{F}_i}{\delta\xi} + \frac{\delta\vec{G}_i}{\delta\eta} + \frac{\delta\vec{H}_i}{\delta\zeta} - \frac{1}{Re}\left[\frac{\delta\vec{F}_v}{\delta\xi} + \frac{\delta\vec{G}_v}{\delta\eta} + \frac{\delta\vec{H}_v}{\delta\zeta}\right] = \vec{S}$$

The solution vector $\vec{Q} = [\rho, \rho u, \rho v, \rho w, \rho e]^T$ gives the solution variables in conservative form in order to better preserve continuity. Specific energy is solved separately.

$$e = \frac{T}{\gamma(\gamma-1)M_\infty^2} + \frac{1}{2}\,(u^2 + v^2 + w^2\,)$$

Finally, the perfect gas relation is used to find pressure.

$$p = \frac{\rho T}{\gamma M_\infty^2}$$

Inviscid flux terms are defined as vectors $\vec{F}_i$, $\vec{G}_i$, and $\vec{H}_i$.

$$\vec{F}_i = \begin{bmatrix} \rho\hat{u} \\ \rho u\hat{u} + \xi_x p \\ \rho v\hat{u} + \xi_y p \\ \rho w\hat{u} + \xi_z p \\ (\rho e + p)\hat{u} - \xi_t p \end{bmatrix} \quad \vec{G}_i = \begin{bmatrix} \rho\hat{v} \\ \rho u\hat{v} + \eta_x p \\ \rho v\hat{v} + \eta_y p \\ \rho w\hat{v} + \eta_z p \\ (\rho e + p)\hat{v} - \eta_t p \end{bmatrix} \quad \vec{H}_i = \begin{bmatrix} \rho\hat{w} \\ \rho u\hat{w} + \zeta_x p \\ \rho v\hat{w} + \zeta_y p \\ \rho w\hat{w} + \zeta_z p \\ (\rho e + p)\hat{w} - \zeta_t p \end{bmatrix}$$

The metric quantities are given as $\xi_x,\ \xi_y,\ \xi_z$, and ξ_t.

$$\xi_x = (J^{-1})\delta\xi/\delta x$$

$$\xi_y = (J^{-1})\delta\xi/\delta y$$

$$\xi_z = (J^{-1})\delta\xi/\delta z$$

$$\xi_t = (J^{-1})\delta\xi/\delta t$$

The transformation Jacobian is defined by $J = \delta(\xi, \eta, \zeta, \tau)/\ \delta(x, y, z, t)$ and $\hat{u}$, $\hat{v}$, and $\hat{w}$ are the transformed flow velocity components.

$$\hat{u} = \xi_t + \xi_x u + \xi_y v + \xi_z w$$

$$\hat{v} = \eta_t + \eta_x u + \eta_y v + \eta_z w$$

$$\hat{w} = \zeta_t + \zeta_x u + \zeta_y v + \zeta_z w$$

The viscous flux vectors are given below, where τ_{ij} is the shear stress tensor and b_i is the heat flux tensor. $i = 1,2,3$ is used to form a more compact notation, e.g. x_i represents x, y and z. Pr for air is given as 0.72.

$$\vec{F}_v = \begin{bmatrix} 0 \\ \xi_{x_i}\tau_{i1} \\ \xi_{x_i}\tau_{i2} \\ \xi_{x_i}\tau_{i3} \\ \xi_{x_i}b_i \end{bmatrix} \quad \vec{G}_v = \begin{bmatrix} 0 \\ \eta_{x_i}\tau_{i1} \\ \eta_{x_i}\tau_{i2} \\ \eta_{x_i}\tau_{i3} \\ \eta_{x_i}b_i \end{bmatrix} \quad \vec{H}_v = \begin{bmatrix} 0 \\ \zeta_{x_i}\tau_{i1} \\ \zeta_{x_i}\tau_{i2} \\ \zeta_{x_i}\tau_{i3} \\ \zeta_{x_i}b_i \end{bmatrix}$$

$$\tau_{ij} = \mu\left(\frac{\delta\xi_k}{\delta x_j}\frac{\delta u_i}{\delta\xi_k} + \frac{\delta\xi_k}{\delta x_i}\frac{\delta u_j}{\delta\xi_k} - \frac{2}{3}\delta_{ij}\frac{\delta\xi_l}{\delta x_k}\frac{\delta u_k}{\delta\xi_l}\right)$$

$$b_i = u_j \tau_{ij} + \frac{k}{(\gamma - 1) Pr M_\infty^2} \frac{\delta \xi_l}{\delta x_i} \frac{\delta T}{\delta \xi_l}$$

2.2. Non-Dimensionalization

To aid in consistency among all calculations, all flow variables, except for pressure, are normalized by their respective reference freestream values.

$$T^* = \frac{T}{T_\infty}\ , \rho^* = \frac{\rho}{\rho_\infty}, U_i^* = \frac{U_i}{U_\infty}, M^* = \frac{M}{M_\infty}$$

Pressure is normalized with upstream density and velocity.

$$p^* = \frac{p}{\rho_\infty U_\infty^2}$$

Finally, the spatial dimensions are normalized by the chord length.

$$x^* = \frac{x}{c}, y^* = \frac{y}{c}, z^* = \frac{z}{c}$$

Time and actuation frequency are scaled with both chord length and upstream velocity.

$$t = \tau c / u_\infty,\ f = \omega_a 2\pi c / u_\infty$$

2.3. Numerical Discretization

A finite-differencing approach is used to discretize the governing Navier–Stokes Equations, while a high-order compact-differencing scheme is used to obtain all spatial derivatives developed by (Gaitonde & Visbal, 1998). On the interior of the computation domain, any scalar quantity, ϕ such as a spatial, flux component, or flow variable, the spatial derivatives ϕ' may be obtained at the node points in the computation space by solving the tridiagonal system for a five point stencil.

$$\alpha \phi'_{i-1} + \phi'_i + \alpha \phi'_{i+1} = \beta \frac{\phi_{i+2} - \phi_{i-2}}{4} + \Gamma \frac{\phi_{i+1} - \phi_{i-1}}{2}$$

Where α, β, and Γ are used to define the algorithm's spatial properties. Based on the sixth-order scheme used in this research, α, β, and Γ are defined as 1/3, 1/9, and 14/9 respectively. At boundary points, higher-order one-sided formulas are utilized which retain the tridiagonal form of the scheme. At the grid boundaries, for the first and last points in the x-, y-, and z-direction the code utilizes a fourth-order compact (C4) scheme and a seven point stencil. First the value at the boundary surface (point 1) is calculated.

$$\phi_1' + \alpha_1\phi_2' = a_1\phi_1 + b_1\phi_2 + c_1\phi_3 + d_1\phi_4 + e_1\phi_5 + f_1\phi_6 + g_1\phi_7$$

Eight coefficients are needed for the chosen scheme.

$$\alpha_1 = 3, a_1 = \frac{-17}{6}, b_1 = \frac{3}{2}, c_1 = \frac{3}{2}\ d_1 = \frac{-1}{6}, e_1 = 0, f_1 = 0, g_1 = 0$$

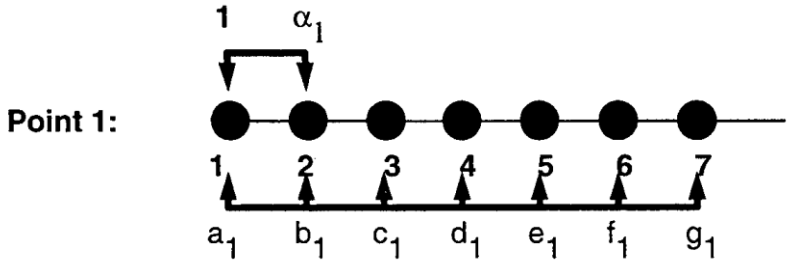

Figure 2.1. Point 1 Boundary Stencil (Gaitonde & Visbal, 1998).

Next the value next to the boundary surface (point 2) is calculated.

$$\alpha_{21}\phi_1' + \phi_2' + \alpha_{22}\phi_3' = a_2\phi_1 + b_2\phi_2 + c_2\phi_3 + d_2\phi_4 + e_2\phi_5 + f_2\phi_6 + g_2\phi_7$$

Nine coefficients are needed for the chosen scheme.

$$a_{21} = \frac{3}{14}, a_{22} = \frac{3}{14}, a_2 = \frac{-19}{28}, b_2 = \frac{-5}{42}, c_2 = \frac{6}{7}\ d_2 = \frac{-1}{14}, e_2 = \frac{1}{84},\ f_2 = 0, g_2 = 0$$

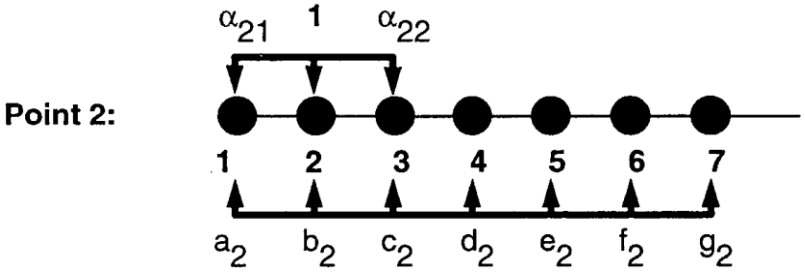

Figure 2.2. Point 2 Boundary Stencil (Gaitonde & Visbal, 1998).

2.4. Time Marching

Time marching is accomplished by incorporating a second-order iterative, implicit approximately-factored method of Beam and Warming as described, e.g., in (Visbal & Gaitonde, 2002) and (Visbal et al., 2003). This method gives the Jacobian second-order accuracy while the other side is evaluated with the compact differencing high-order method. The scheme is given in second-order delta form.

$$\left[J^{-1^{p+1}} + \phi^i \Delta\tau \delta_\xi^{(2)} \left(\frac{\partial \hat{F}^p}{\partial U} - \frac{1}{Re}\frac{\partial \hat{F}_v^p}{\partial U}\right)\right] J^{p+1}$$

$$\times \left[J^{-1^{p+1}} + \phi^i \Delta\tau \delta_\xi^{(2)} \left(\frac{\partial \hat{G}^p}{\partial U} - \frac{1}{Re}\frac{\partial \hat{G}_v^p}{\partial U}\right)\right] J^{p+1}$$

$$\times \left[J^{-1^{p+1}} + \phi^i \Delta\tau \delta_\xi^{(2)} \left(\frac{\partial \hat{H}^p}{\partial U} - \frac{1}{Re}\frac{\partial \hat{H}_v^p}{\partial U}\right)\right] \Delta\hat{U}$$

$$= -\phi^i \Delta\tau \left[J^{-1^{p+1}} + \frac{(1+\phi)U^p - (1+2\phi)U^n + \phi U^{n-1}}{\Delta\tau} + U^p (1/J)_\tau^p \right.$$

$$\left. + \delta_\xi \left(\hat{F}^p - \frac{1}{Re}\hat{F}_v^p\right) + \delta_\eta \left(\hat{G}^p - \frac{1}{Re}\hat{G}_v^p\right) + \delta_\zeta \left(\hat{H}^p - \frac{1}{Re}\hat{H}_v^p\right)\right]$$

$\partial\hat{F}/\partial U$, $\partial\hat{G}/\partial U$, and $\partial\hat{H}/\partial U$ are flux Jacobians, with δ representing the spatial difference operator, $\phi^i = 1/(1+\phi)$ and $\Delta\vec{U} = \vec{U}^{p+1} - \vec{U}^p$. This method combines both approximate factorization procedure and diagonalized simplification. This method also

has nonlinear dissipation terms that have been lumped into the implicit operator to aid in stability. Errors due to linearization, diagonalization, and explicit boundary condition implementation are eliminated by the use of sub-iterations represented by the superscript p, of which three are applied per time step. Thus, for the first sub-iteration, $p = 1$, $\vec{U}^p = \vec{U}^n$ and as $p \to \infty, \vec{U}^p = \vec{U}^{n+1}$. By changing the number of time levels employed to evaluate the time-derivative term, first- and third-order accurate forms of the implicit algorithm can be constructed. This also eliminates the impact of the implicit damping coefficients on the final solution (Visbal & Gaitonde, 2002).

2.5. Filtering

Compact schemes, like other centered schemes, are non-dissipative and therefore susceptible to numerical instabilities due to unrestrictive growth of high frequency modes. The instabilities can arise from non-uniformity in the grid, the boundary conditions, and nonlinearity in the fluid flow. In LES, where the scales at which physical viscous dissipation occurs are not represented, the use of a non-dissipative scheme leads to the pile-up of energy at the high wave numbers of the mesh and ultimately to numerical instability. The code therefore uses a high-order implicit Pade-type filtering technique (Visbal & Gaitonde, 2002) to dampen these instabilities. The formula for the interior filtering is very similar to the equation for interior solutions.

$$\alpha_f \hat{\phi}_{i-1} + \hat{\phi}_i + \alpha_f \hat{\phi}_{i+1} = \sum_{n=0}^{F} \frac{a_n}{2} (\phi_{i+n} - \phi_{i-n})$$

Where $\hat{\phi}$ denotes filtered values and ϕ represents unfiltered values. The filter allows for different orders of accuracy to be used, denoted by $2F$. This results in $n = F + 1$ coefficients or $a_0, a_1, \ldots a_n$, which are derived using Taylor- and Fourier-series analyses.

In order for the filter to successfully dampen the evolving poorly resolved high-frequency content of the solution, the scheme must be at least 2 orders higher than that of the difference scheme that is being implemented. For the sixth-order discretization scheme used on the interior grid points, the filter must be eighth-order accurate. To achieve this, six coefficients are required.

$$a_0 = \frac{93 + 70\alpha_f}{128},\ a_1 = \frac{7 + 18\alpha_f}{16},\ a_2 = \frac{-7 + 14\alpha_f}{32},$$

$$a_3 = \frac{1}{16} - \frac{\alpha_f}{8},\ a_4 = \frac{-1}{128} - \frac{\alpha_f}{64},\ a_5 = 0$$

The additional coefficient α_f may be used to control the spectral response of the filter by setting the value in the range $-0.5 < \alpha_f < 0.5$, where a higher value corresponds to less dissipative filtering with 0.5 resulting in no filtering. Implicit filtering is enabled when $\alpha_f \neq 0$, where $\alpha_f = 0$ results in explicit filtering. For the filtering of interior grid points, $\alpha_f = 0.4$.

2.6. Computational Meshes

A 1293 × 789 × 3 mesh generated around a Joukowski symmetric airfoil with 12% chamber is employed and shown in Figure 2.3, with a view of the embedded SJA in Figure 2.4 A highly stretched region in the far field is used to dampen any spurious reflected waves. The mesh was previously validated in our earlier work (Golubev et al., 2015; Mankbadi et al., 2015). Such a fine near-field mesh is required to provide an accurate resolution of the boundary-layer vorticity dynamics and acoustic waves which at certain flow conditions may interact to form a self-sustained feedback loop. This resonance mechanism was experimentally and numerically explored by (Golubev et al.,

2014) for a NACA 0012 airfoil. The resonance was also suspected to dominate the trailing-edge noise radiation observed at a transitional flow regime over a Joukowski airfoil investigated in (Golubev et al., 2011; Golubev et al., 2010b). The current study focuses on this flow regime to confirm this assumption and examine in more detail the features of the suspected flow-acoustic resonant interaction. An additional regime is tested using the previously validated (Golubev et al., 2014) NACA 0012 mesh at a lower speed and high-Re to test the robustness of this control method. Its nearfield and SJA regions are nearly identical to those of the Joukowski mesh shown in Figure 2.3 and Figure 2.4.

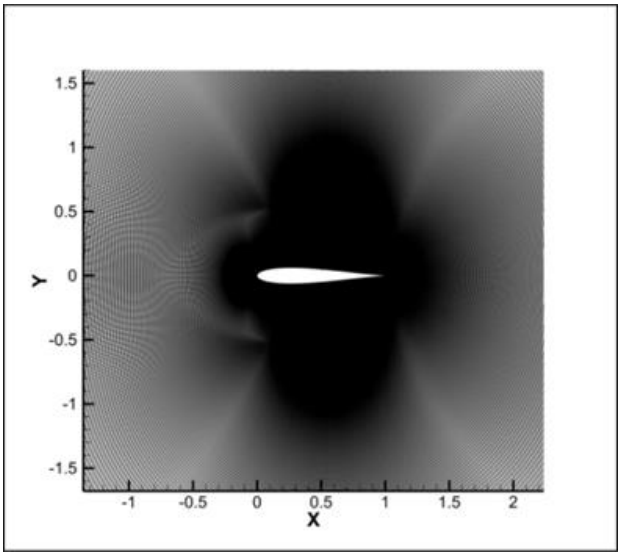

Figure 2.3. Sectional Mesh Near The Airfoil Surface.

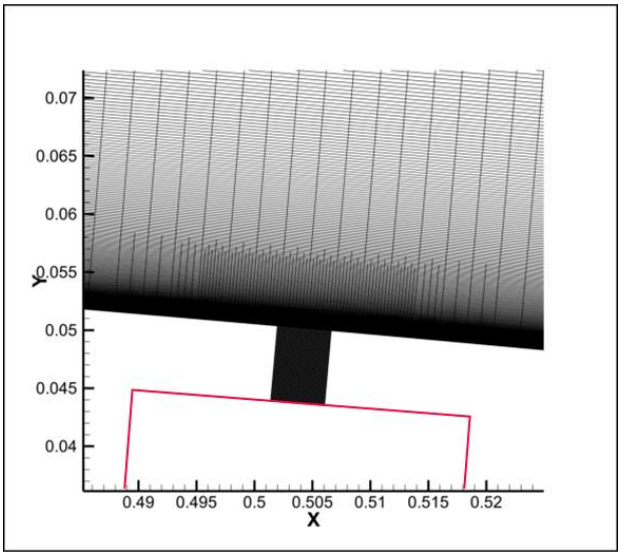

Figure 2.4. Details Of Overset Meshes In SJA Orifice Region.
Red Outline Represents The Cavity Which Is Ignored And Not Modelled.

A Synthetic-Jet Actuator (Glezer, Ari & Amitay, 2002), as shown in Figure 1.5, is a zero net mass device that oscillates a piezo-electric membrane to produce a stream of air. Modeling of the SJA is realized through embedding the orifice mesh in the airfoil surface and providing an adequate overlap with the original airfoil mesh, as shown in Figure 2.4. The proper implementation of the employed overset grid methodology involves 6 meshes generated using Pointwise© software in the near-orifice overlap region. The overset grid connectivity is established using NASA's PEGASUS (Suhs et al., 2002) and AFRL's BELLERO (Sherer et al., 2006) software, with the connectivity data produced by the former serving as input for the latter handling grid decomposition and establishing the inter-grid communication required for the grid system, subdivided into blocks for parallel processing. More details of the employed overset mesh procedures can be found in (Sherer et al., 2006). This overset method allows us to keep the structured O-grid mesh unchanged and perfectly model the orifice corners. Without this method the orifice corners would impact the orthogonality of the grid and increase

numerical error. The indices of all meshes used for both airfoils are listed in Table 2.1 and Table 2.2.

Table 2.1. Joukowski Mesh Indices.

Mesh #	I-Index	J-Index	K-Index
1 (O-grid)	1293	789	3
2	19	60	3
3	29	58	3
4	41	56	3
5	65	54	3
6 (Orifice)	33	129	3

Table 2.2. NACA Mesh Indices.

Mesh #	I-Index	J-Index	K-Index
1 (O-grid)	1281	789	3
2	17	125	3
3	29	120	3
4	41	115	3
5	49	110	3
6 (Orifice)	33	140	3

In the majority of cases employed in this study, the embedded actuator model is positioned at the airfoil midchord on the upper surface, with the effect of SJA location further addressed in Section 3.3. This location is near where separation starts and viscous effects must be considered. The ratio of the orifice width to the airfoil chord in this study is fixed at d/c=0.005.

2.7. Boundary Conditions

The boundary condition specified along the airfoil surface is a no-slip, adiabatic wall with fourth-order extrapolation. A periodicity condition is imposed at the span end planes and overlapped region adjacent to the leading edge. At the outer O-grid boundary,

a freestream condition is applied to the farfield with the grid rapidly stretching towards the boundary to ensure effective elimination of spurious reflections achieved in conjunction with the low-pass spatial filtering. In the case of overset meshes, only periodicity conditions are imposed at the span end planes, while the circumferential and normal faces are interpolated from the original mesh.

The SJA orifice mesh is embedded in the airfoil surface with a five point interpolated overlap region, with wall boundary conditions applied at the sides and the bottom of the orifice. This represents the geometry change due to the addition of the SJA, with the absence of the full cavity for simplification. Note that such approach accounts for the effect of synthetic-jet interaction with grazing flow that modifies the jet structure at the orifice exit, which thus precludes specifying fluctuating jet velocity directly at the orifice's exit (i.e., on the airfoil surface). (Raju et al., 2009) suggested that imposing a simple time-harmonic velocity fluctuation thus achieves good comparison with results obtained from simulations with a complete actuator model. A single velocity component normal to the orifice bottom is considered in the current work, which produces the following simple expression for the resulting fluctuating velocity at the bottom of the orifice, give as $v_{SJA} = v_m \cos(\omega_a t)$. This condition replaces the bottom wall boundary condition for cases where the actuator is activated.

3. Results-Joukowski High Speed Regime

We consider a 12%-thick Joukowski airfoil with a chord length of 0.1m at Mach number $M = 0.5$ with $Re = 5 \times 10^4$ (Scott, 2004). The resulting Re within the cavity is calculated to be approximately 125 due to the small length scale. Calculations are performed with a non-dimensional time step τ of 9×10^{-5}, dimensionalized by $t = \tau c/u_\infty$. The resulting CFL number is calculated as 0.057, much less than the standard value of 1 needed for explicit schemes. In practice, the time step is kept low from experience with errors that occur at higher time steps. For each case, the mesh is partitioned into 700 overlapped blocks assigned to different processors to be solved in parallel. The total runtime approaches 10 hours of clock time, or 7,000 CPU hours. A total of 16384 samples are recorded skipping every 44 iterations after a quasi-steady state is achieved. Due to the periodic nature of the flow, a true steady-state will not be reached. The flow is determined to be quasi-steady when the lift begins to show a periodic sinusoidal pattern. SJA actuation is set to non-dimensional amplitude $v_m = 0.5$, correlating to half of the upstream velocity, and non-dimensional frequency values set to $\omega_a = 9, 10.47, 12, 15, 18, 21$. These values correspond to the dimensionalized frequency f with $f = \omega_a 2\pi c/u_\infty$. Calculated from the equation for kinetic energy of pipe flow, $KE = 1/2\rho AS$, the resulting flow injects approximately 1.5mJ per meter span of energy into the boundary layer. The case with the actuation frequency of 10.47 is meant to match the vortical shedding of the clean airfoil, calculated from the Strouhal Number 0.2. Cases will be referred to as “clean” if no SJA is implemented, “cavity” if the SJA cavity is implemented with no actuation, representing only the geometry change, and “actuation” when the SJA is fully activated. The full list of cases is shown in Table 3.1.

Table 3.1. Joukowski Airfoil Test Case Descriptions.

Case Type	Case Name
Unaltered Joukowski Airfoil	Clean
Joukowski Airfoil With Non-actuating Cavity	Cavity
Joukowski Airfoil With Actuating Cavity	Actuation $\omega_a = 9$
Joukowski Airfoil With Actuating Cavity	Actuation $\omega_a = 10.47$
Joukowski Airfoil With Actuating Cavity	180° Out Of Phase Actuation $\omega_a = 10.47$
Joukowski Airfoil With Actuating Cavity	Actuation $\omega_a = 12$
Joukowski Airfoil With Actuating Cavity	Actuation $\omega_a = 15$
Joukowski Airfoil With Actuating Cavity	Actuation $\omega_a = 18$
Joukowski Airfoil With Actuating Cavity	Actuation $\omega_a = 21$

3.1. Actuation Effects on the Flow Field

Time-averaged solutions of the flow field for the clean, cavity and actuation case with frequency $\omega_a = 9$ are examined first. Figure 3.1, Figure 3.2 and Figure 3.3 represent the time-averaged solution of the z-vorticity at the trailing edge, negative u-velocity at the trailing edge and the z-vorticity at the orifice location respectively. z-vorticity represents the spin of the flow and is used to easily show the existence of vortices, as well as approximating the thickness of the boundary layer. Results show the clean case regime features a very thick boundary layer, measuring approximately 6.5% of the chord at the trailing edge. Zones of recirculation/separation also appear on both sides of the airfoil from the trailing edge up till midchord. Comparison with the cavity case shows the boundary layer thickness decreases to 4.5% chord on the bottom.

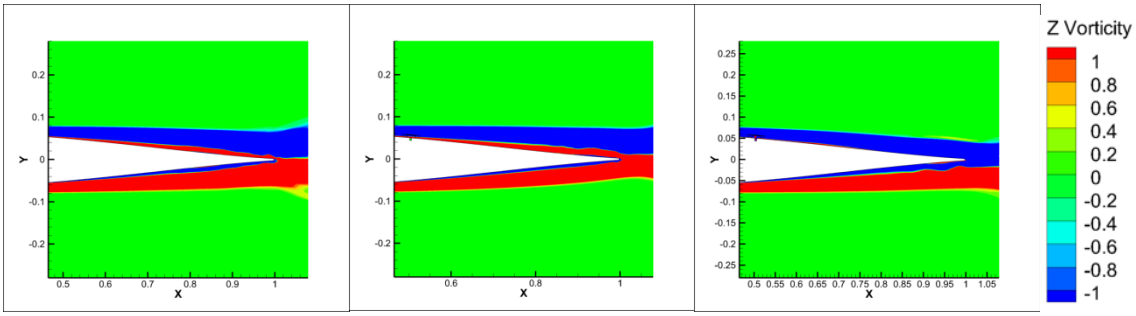

Figure 3.1. Average z-Vorticity Contours.
Clean (Left), Cavity (Middle), Actuating (Right).

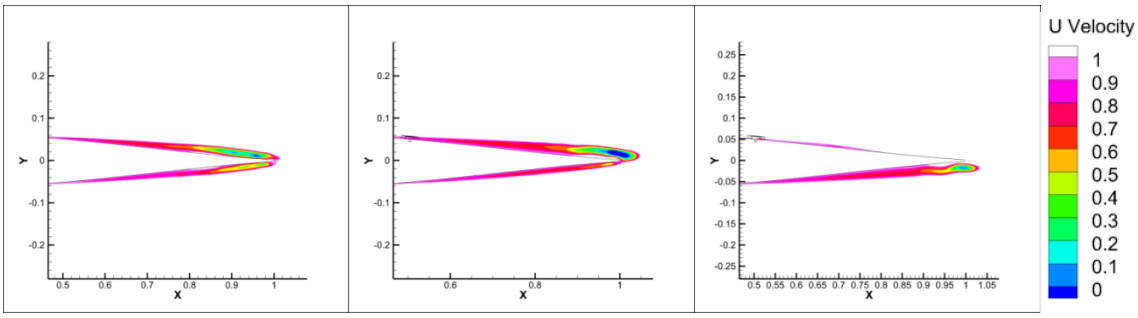

Figure 3.2. Average Negative u-Velocity Contours Showing Recirculation. Clean (Left), Cavity (Middle), Actuating (Right).

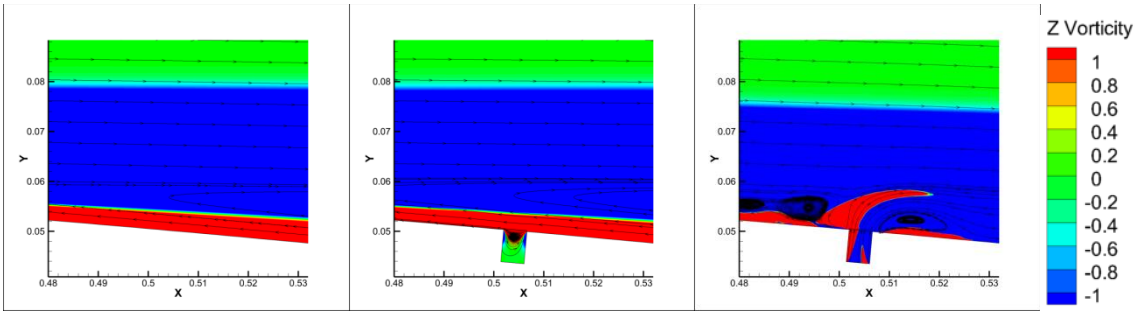

Figure 3.3. Instantaneous z-Vorticity Contours At SJA location At τ=121. Clean (Left), Cavity (Middle), Actuating (Right).

3.2. Actuation Effects on the Surface

Although the purpose of using SJAs is for a control method for noise reduction, the data suggests that they can improve lift performance as well. We see again in Figure 3.4 that the change in geometry from the non-actuating SJA causes only a small change in both C_p and P_{RMS} on the surface. In Figure 3.5 we can observe the small performance boost in lift. With actuation at frequency $\omega_a = 9$, the mean pressure on the top surface is reduced while the mean pressure on the bottom surface is increased, resulting in the significant increase in average lift seen in Figure 3.5. Its effects even propagate to the leading edge.

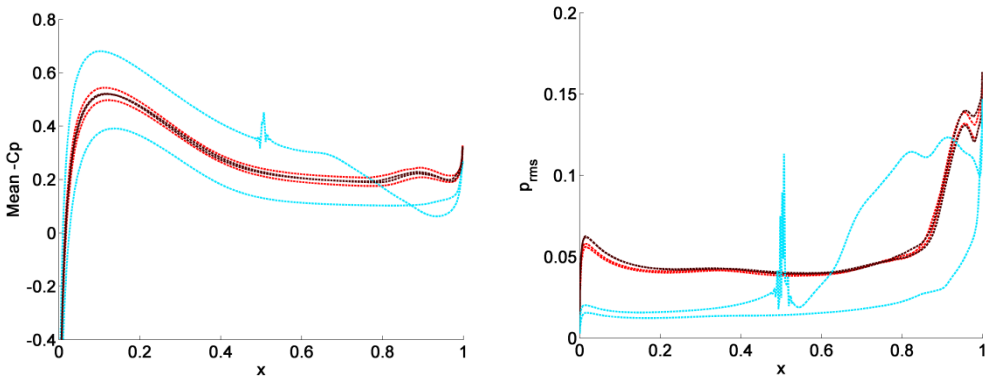

Figure 3.4. Surface Pressure On Surface For Joukowski Cases.
Mean – Cp (left), And P_{RMS} (Right).
Clean (Red), No Actuation Cavity (Black), Frequency 9 (Cyan).

A spike can be observed at the SJA location. This is accompanied by a lower P_{RMS} for everywhere but the top side trailing edge resulting in a much smoother and regularized unsteady lift history indicated by the smaller fluctuation amplitude seen in Figure 3.5. Comparison to the previous data shows similar levels for the lift on the clean and cavity cases, with some variation due to the difference in time the cases took to reach a quasi-steady state. This is due to the code being updated to the most current version. The lower levels in the old data for the lift under actuation are due to a slight error in the SJA velocity boundary, which was set to a slight angle. This was rectified in the current study. The dominant frequencies for the lift are shown in Figure 3.6. For the clean and cavity cases, there exists a low frequency peak that corresponds with the long period lift oscillation. The cases are not run for long enough to resolve the exact frequency. More importantly, another peak is shown at about 3000Hz. This correlates exactly with the predicted non-dimensional shedding frequency of 10.47. For the actuation case, both the low frequency tone and the shedding tone are dampened and replaced with a lower magnitude tone at about 2600Hz which matches the non-dimensional actuation frequency of 9. Looking at the time derivative of lift in Figure 3.7, we see again that there is little

change with the inclusion of the orifice. However, with actuation there is a drop-off in mean amplitude from about 8.4×10^{-4} to 4.5×10^{-4}. This relates to the drop-off of dipole strength. Unfortunately, the inclusion of the cavity appears to have a negative effect on drag as shown in Figure 3.8. Due to the flow grazing past the SJA orifice, average drag increases from $C_d = 0.03186$ to $C_d = 0.04822$. When actuation is introduced, drag decreases slightly to $C_d = 0.04307$, but this is still higher than the clean case drag. Looking now at the mean surface friction in Figure 3.9, we see once again minor differences between the clean case and cavity cases, with the exception of a spike appearing at the orifice location. An initial separation point at around 40% chord appears where the skin friction becomes negative. The flow then briefly reattaches at 80% chord, but quickly separates again until just before the trailing edge. With actuation, the initial separation point is delayed to 45% chord. The flow reattaches again around 80% chord, but stays attached afterwards unlike the clean and cavity cases.

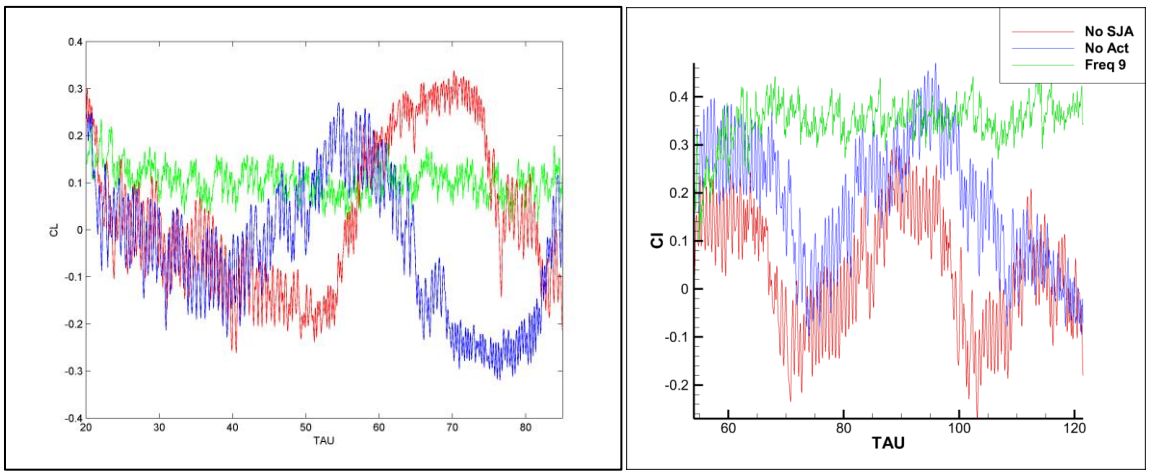

Figure 3.5. Joukowski Lift Histories.
Previous Results (Mankbadi et al., 2014) (Left), Current Results (Right).
Clean (Red), No Actuation Cavity (Blue), Actuation For $\omega_a = 9$ (Green).

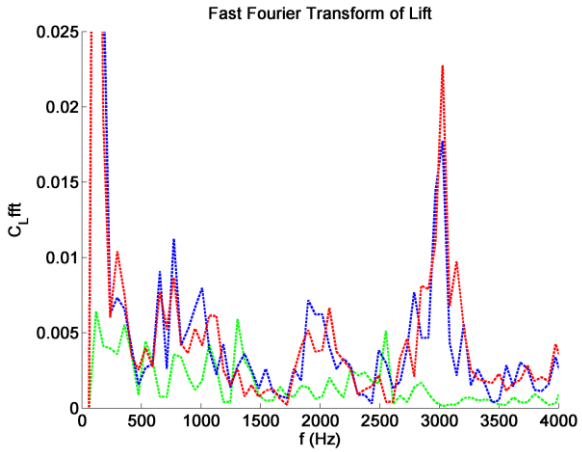

Figure 3.6. FFT Of Lift.
Measurement From Peak At τ=60 To Peak at τ=90.
Clean (Red), No Actuation Cavity (Blue), Actuation for $\omega_a = 9$ (Green).

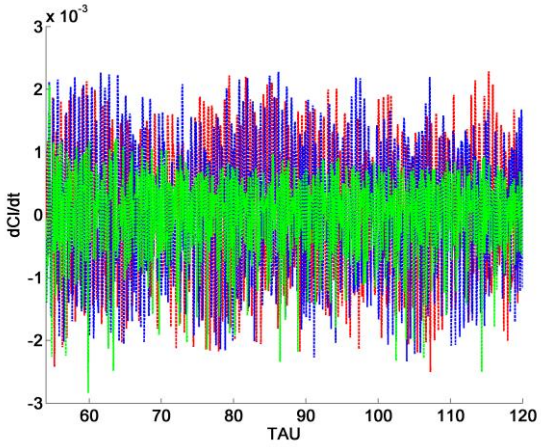

Figure 3.7. Time Derivative Of Lift Histories.
Clean (Red), No Actuation Cavity (Blue), Actuation For $\omega_a = 9$ (Green).

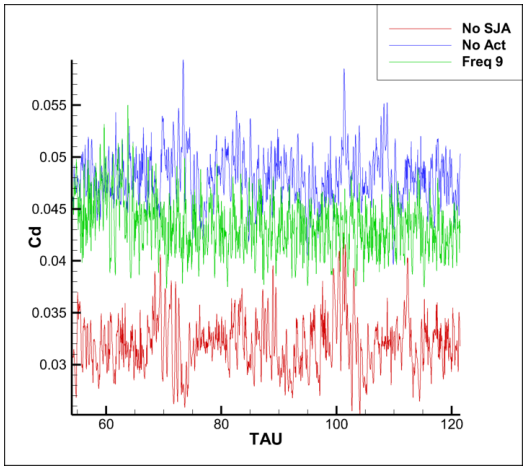

Figure 3.8. Joukowski Drag Histories.
Clean (Red), No Actuation Cavity (Blue), Actuation For $\omega_a = 9$ (Green).

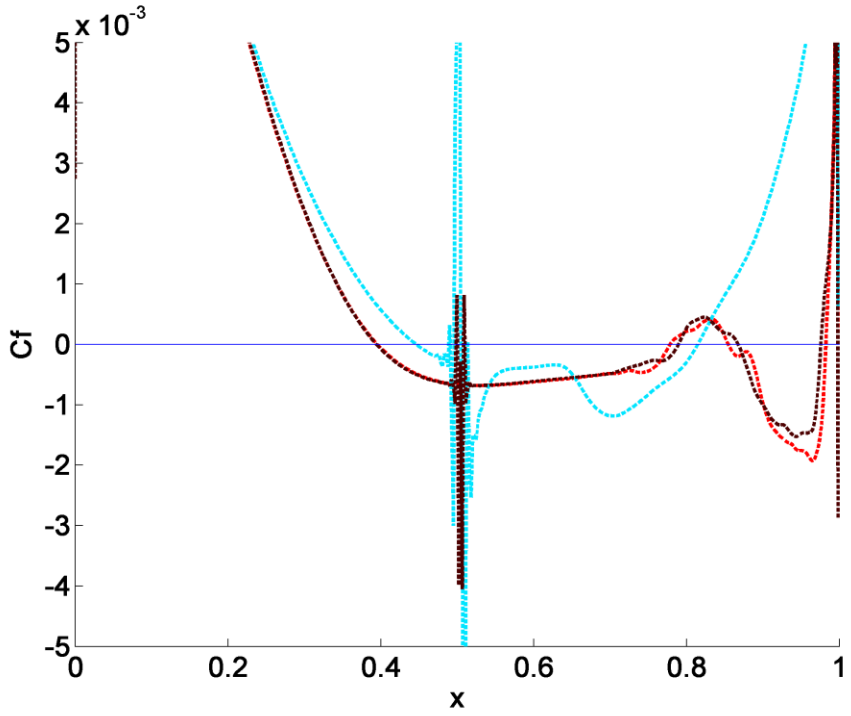

Figure 3.9. Mean Surface Friction Along Top Surface.
Clean (Red), No Actuation Cavity (Black), Frequency 9 (Cyan).

Comparing the average lift increase for each case in Figure 3.10, a trend can be observed of increasing efficiency leading to a local maximum, a decrease as the test frequency approaches the shedding frequency, another increase to a second local maximum, and finally a severe drop. The first local maximum suggests that higher frequencies are not required for more efficiency, therefore energy needs can be kept to a minimum. The first drop in efficiency correlates to the test frequency being in phase with the original shedding frequency. This resonance means that there is less disruption of the vorticity formation when compared to the other cases which are more out of phase with the natural shedding frequency. Despite the loss in relative performance however, there is still a net increase from the baseline case. An additional case is included which incorporates a 180° phase shift for the actuation frequency at 10.47. This case is shown as red in Figure 3.10 and shows that the flow becomes phase locked and shows little change

compared to the case with no phase shift. Moving away from the natural shedding frequency, efficiency rises again up to a critical point, after which energy being introduced into the flow begins to negate any positive effects.

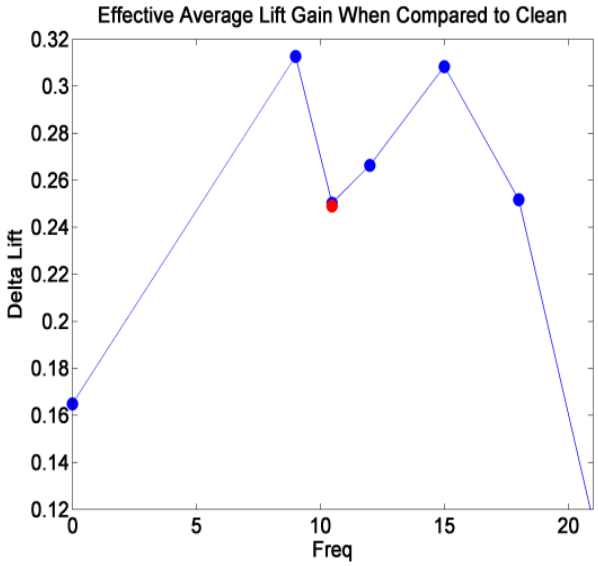

Figure 3.10. Average Lift Gain For Joukowski Cases.
Measurement From Peak τ=60 To Peak at τ=90.
Additional Out Of Phase Case In Red.

3.3. Actuation Effects on Noise

It was already shown by (Sewell, 2012; Mankbadi et al, 2014; Golubev et al., 2015) that an actuating SJA dampens the trailing edge noise of a transitional airfoil by interfering with the transitional switching of the separation vortices. This work now expands on that data with a focus on the effect of actuation frequency. Figure 3.11 shows that for all tested frequency cases, the trailing edge noise measured in a circle with radius $r/c = 1$ was successfully dampened. This is consistent with all prior results (Sewell, 2012; Mankbadi et al, 2014; Golubev et al., 2015) seen in Figure 1.8, with the exception of the non-actuating cavity case which does not appear to significantly change the flow.

Plotting the drop in peak dB levels with comparison to the clean case gives a trend that matches well with what was seen in the lift trend. Sound levels drop by 12 dB for the lowest tested frequency, followed by a small decrease in efficiency when in resonance with the shedding frequency. Sound levels drop-off again past this resonance until a critical point is reached where energy injected into the flow begins to overpower the original noise generation mechanism. This is seen in Figure 3.12. A benefit of this trend reveals that an optimal frequency exists before the natural shedding tone is reached. Therefore this method does not require the use of the extremely powerful SJAs that would be needed to achieve the higher actuation frequencies. The effect of the geometry change without actuation appears negligible.

We now look at the acoustic spectrum at several points on the airfoil and the nearfield, 1 chord above and below midchord. The P_{fft} harmonics are calculated using Matlab (R2014b) with a discrete Fourier transform command on pressure time histories. No windowing is used due to the limited sample size. In Figure 3.13 and Figure 3.14 we see for the cases with no actuation that the primary tone corresponds with the shedding frequency of 10.47. There is no significant change until actuation is turned on, at which point the peak tone switches to match the actuation frequency, which for the case shown is 9. Harmonics of the main tone also appear on the surface due to the non-linear boundary layer effects. Of note is that the higher harmonics are stronger at the trailing edge and are stronger than the single peak tone seen for the non-actuating cases. This pattern appears for all frequencies as shown in and Figure 3.15 through Figure 3.18. In the nearfield at radius $1c$ above and below midchord, the tone is successfully dampened for all frequencies except for $\omega_a = 21$ which was shown in Figure 3.11 and Figure 3.12

to have minimal noise reduction.

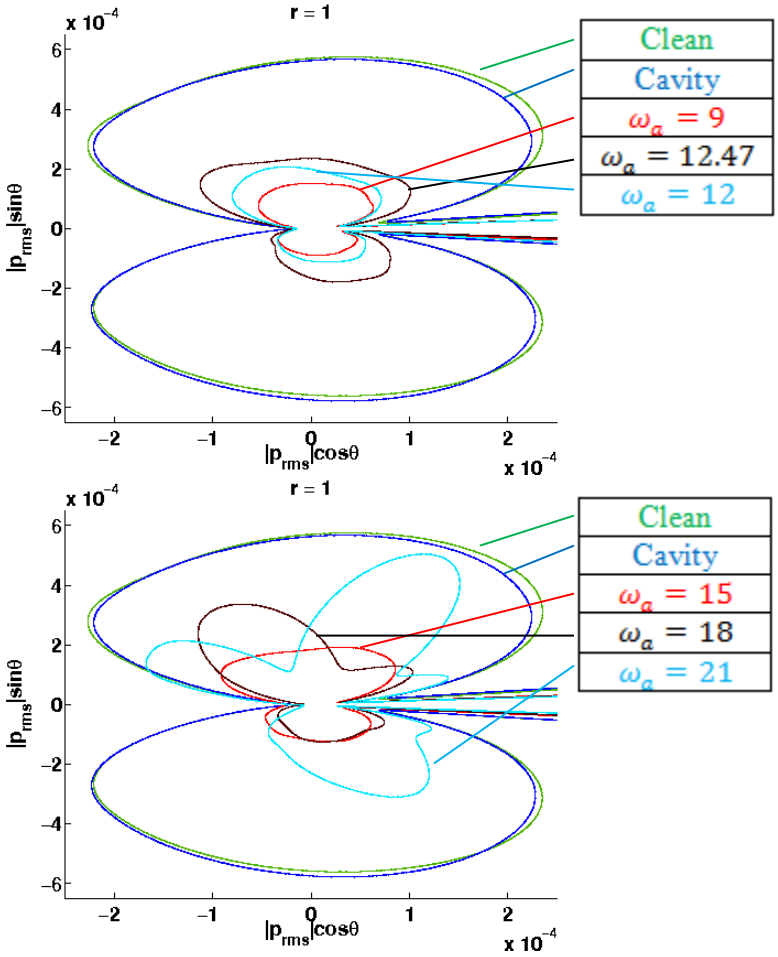

Figure 3.11. P_{rms} Directivities At Radius $1c$ From Chord For Joukowski Cases.
Clean (Green), No Actuation Cavity (Blue).
Frequency 9 (Top Red), 10.47 (Top Black), 12 (Top Cyan),
15 (Bottom Red), 18 (Bottom Black), 21 (Bottom Cyan).

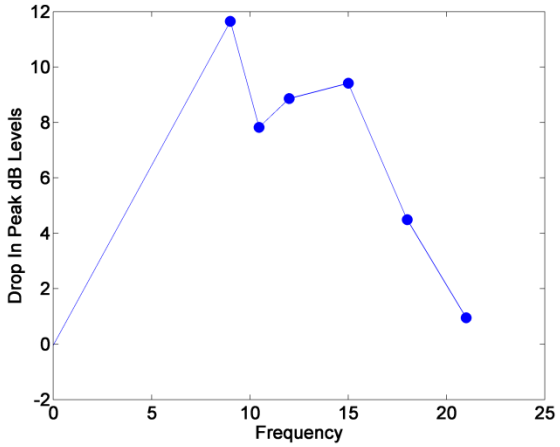

Figure 3.12. Drop In dB Levels For All Frequencies Compared To Clean Case.

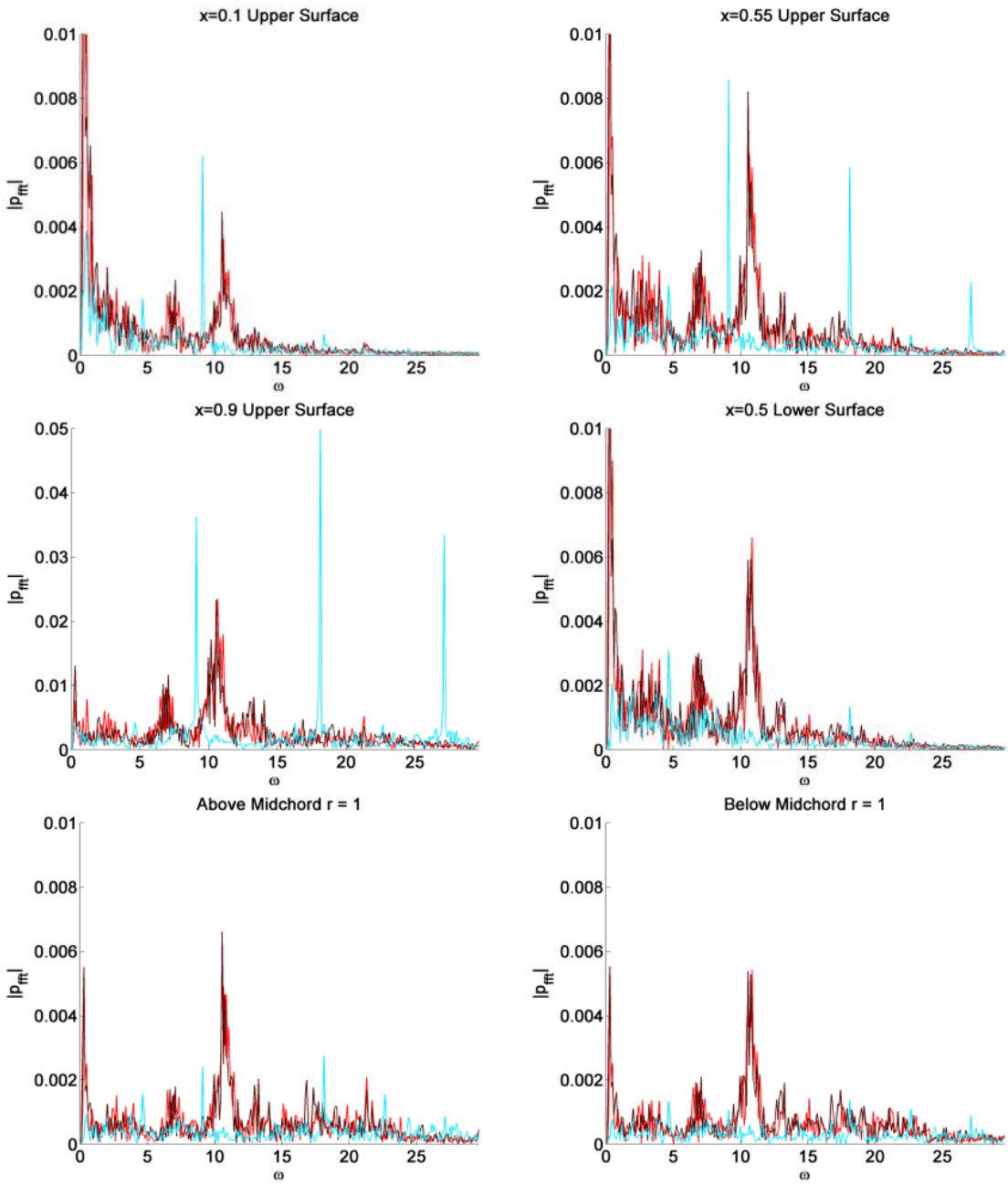

Figure 3.13. Acoustic Spectrum At Various Locations. P_{fft} Vs ω Scale. Clean (Red), No Actuation Cavity (Black), Frequency 9 (Cyan).

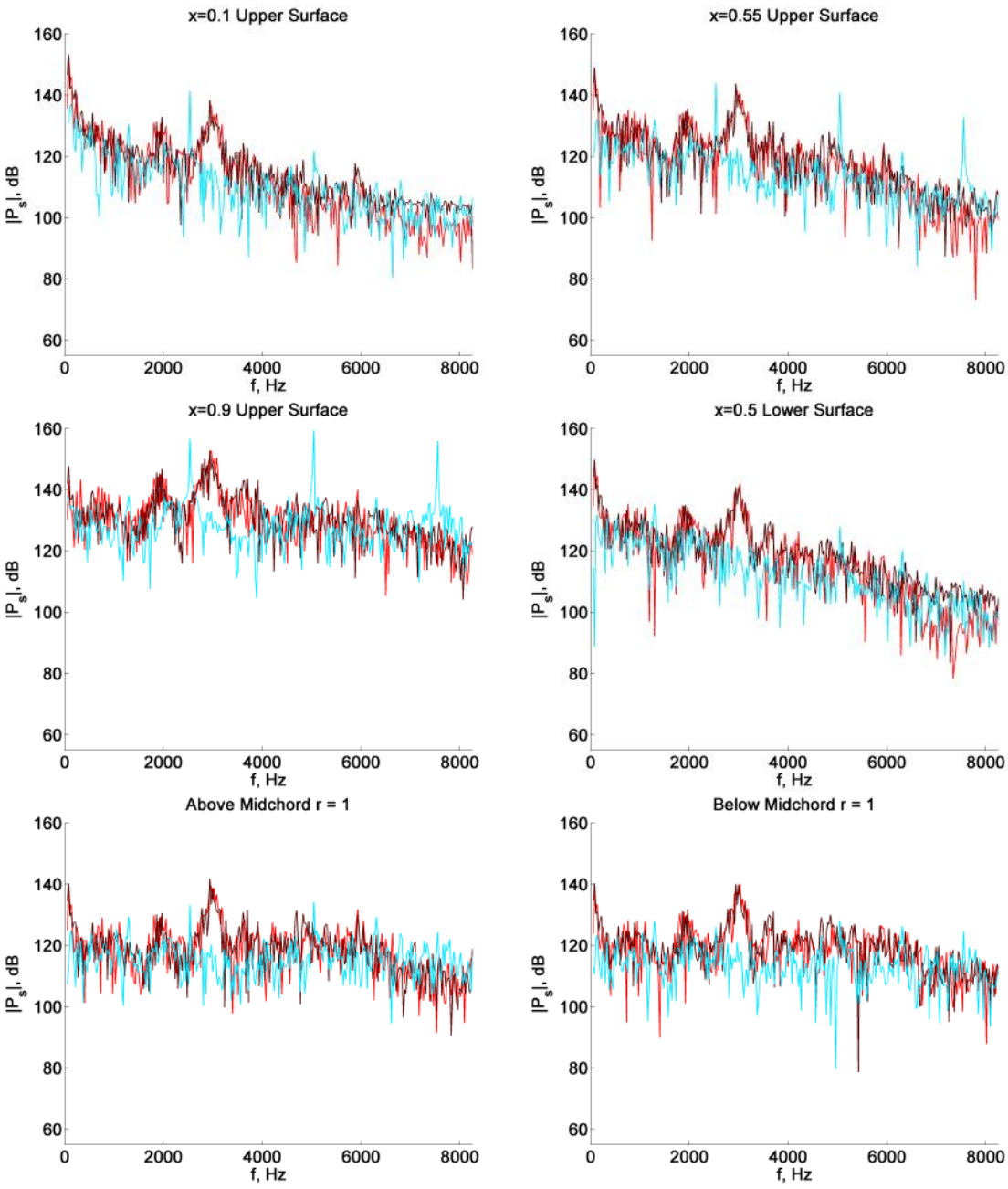

Figure 3.14. Acoustic Spectrum At Various Locations. $dB\ vs\ f$ Scale. Clean (Red), No Actuation Cavity (Black), Frequency 9 (Cyan).

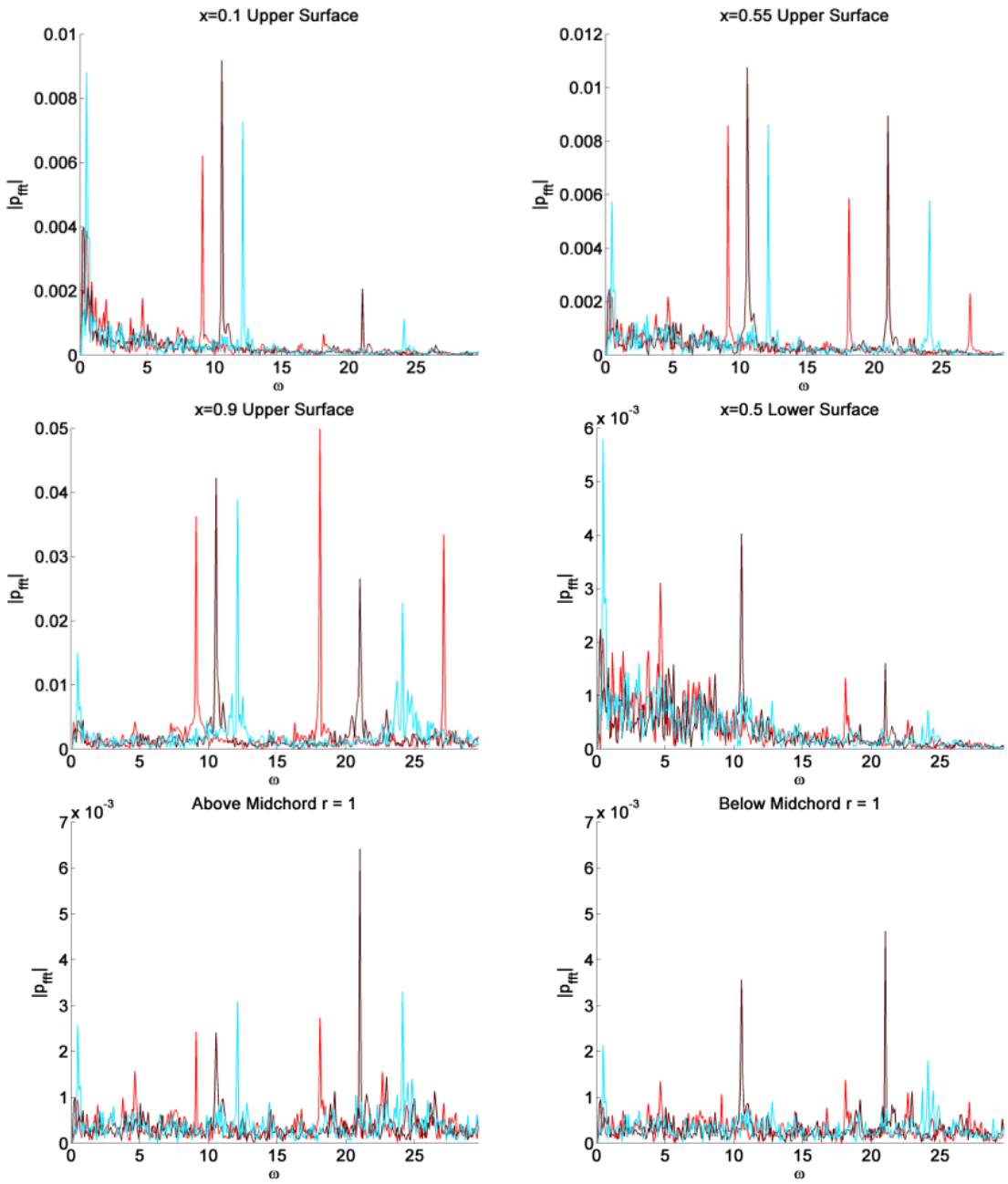

Figure 3.15. Acoustic Spectrum At Various Locations. P_{fft} Vs ω Scale. Frequency 9 (Red), Frequency 10.47 (Black), Frequency 12 (Cyan).

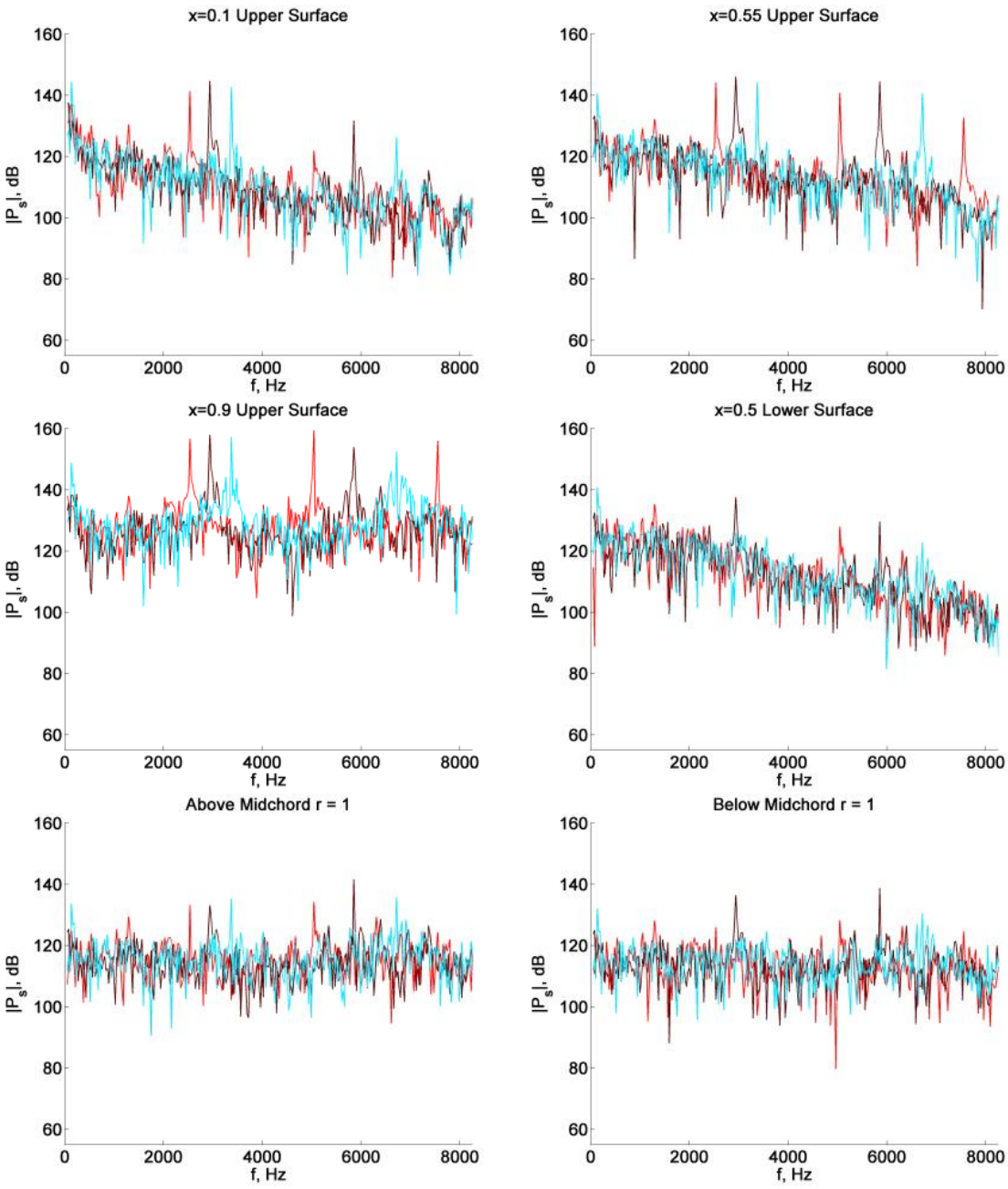

Figure 3.16. Acoustic Spectrum At Various Locations. $dB\ vs\ f$ Scale. Frequency 9 (Red), Frequency 10.47 (Black), Frequency 12 (Cyan).

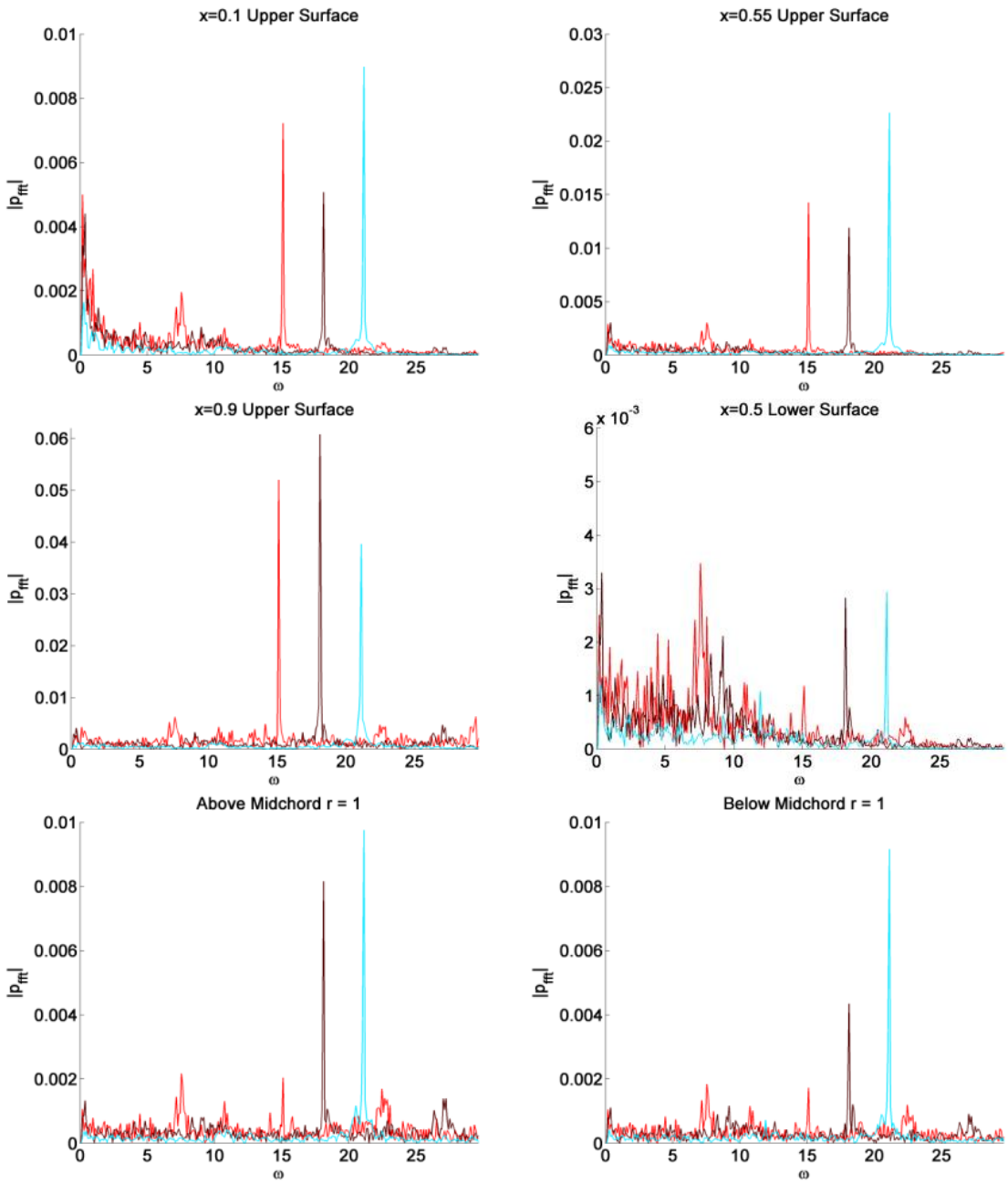

Figure 3.17. Acoustic Spectrum At Various Locations. $P_{fft}\ Vs\ \omega$ Scale. Frequency 15 (Red), Frequency 18 (Black), Frequency 21 (Cyan).

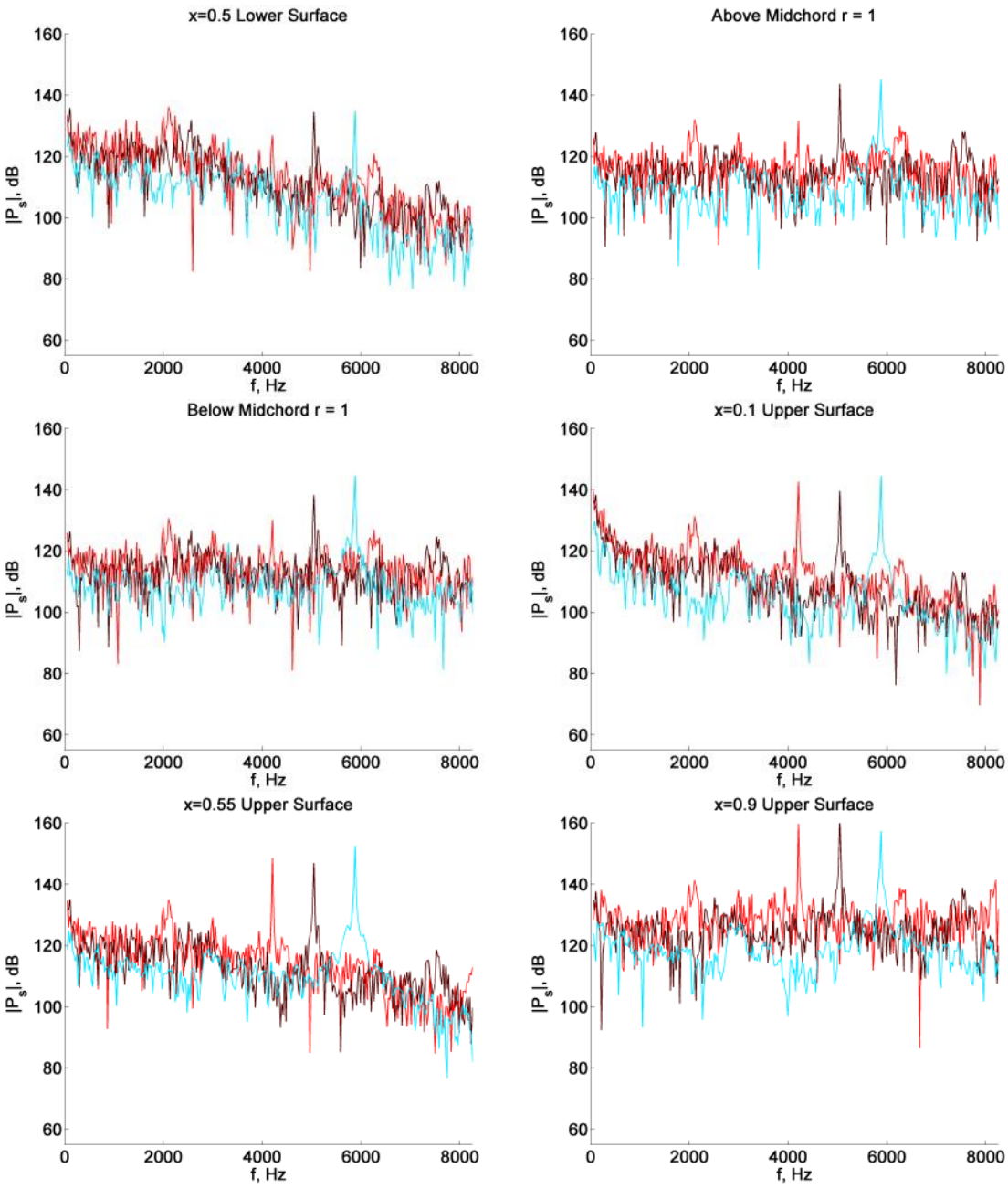

Figure 3.18. Acoustic Spectrum At Various Locations. $dB\ vs\ f$ Scale. Frequency 15 (Red), Frequency 18 (Black), Frequency 21 (Cyan).

3.4. Effect of Synthetic-Jet Actuator Location

Finally, the effect of moving the SJA position near the trailing edge rather than the midchord (as in the previous baseline study) is demonstrated in Figure 3.19 for $\omega_a = 9$. Clearly, the new SJA location fails to disrupt the vortex shedding process and thus shows no significant impact on the airfoil acoustic radiation. It can be concluded that SJA effects must propagate from further upstream in order to impact this process. Although the optimal location must still be determined, it may be concluded that locating the SJA near the midchord separation point is an adequate location for suppression of the airfoil trailing-edge noise for now.

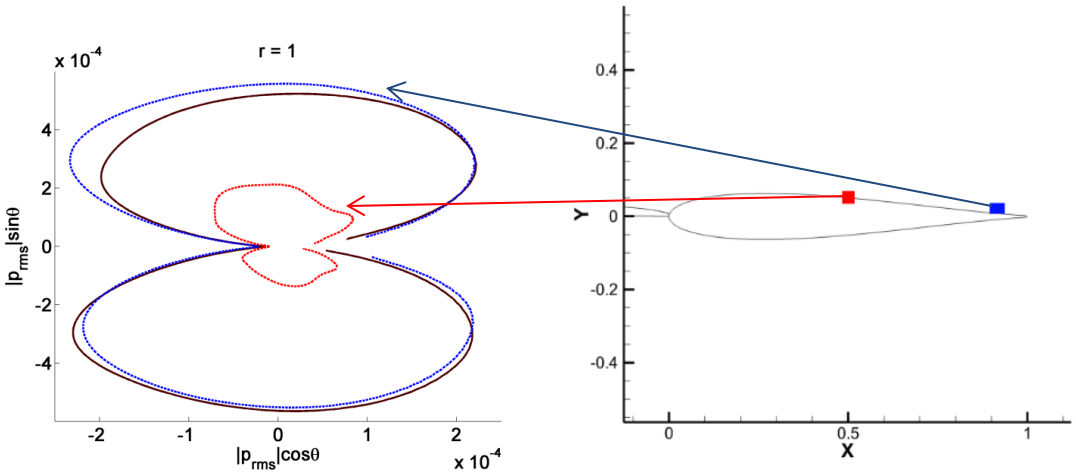

Figure 3.19. Directivities Of P_{RMS} Acoustic Intensity At Radius $1c$.
Clean (Black) Vs. Actuated-Cavity Cases With $\omega_a = 9$.
SJA Located At The Midchord (Red).
SJA Located At The Trailing Edge (Blue). $\omega_a = 9$.

4. Results-NACA Low Speed Regime

In order to test the robustness of this noise control method, we now consider a different regime using a NACA 0012 symmetric airfoil with a chord length of 0.12m at Mach number $M = 0.0465$ with $Re = 1.4 \times 10^5$. The resulting Re within the cavity is calculated to be approximately 450 due to the small length scale. These parameters were chosen to match previously collected data from (Golubev et al., 2015) in order to have some base data to continue from. For each case, the mesh is partitioned into 700 overlapped blocks assigned to different processors to be solved in parallel. The total runtime approaches 10 hours of clock time, or 7,000 CPU hours. Calculations are performed with a non-dimensional time step τ of 4.5×10^{-5}. The resulting CFL number is calculated as 0.088, much less than the standard value of 1 needed for explicit schemes. In practice, the time step is kept low from experience with errors that occur at higher time steps. A total of 16384 samples are recorded skipping every 88 iterations after a quasi-steady state is achieved. SJA actuation is set to non-dimensional amplitude $v_m = 0.5$, correlating to half of the upstream velocity. This is the same scaling used for the Joukowski cases, but it does not take into account the change in Re. A proper scaling factor that compensates for this is currently unknown. Calculated from the equation for kinetic energy of pipe flow, $KE = 1/2\rho AS$, the resulting flow injects approximately 18.1μJ per meter span of energy into the boundary layer. In the 0°AoA case, separation does not occur until 90% chord, so angles of 2°, 4° and 8° are also considered in order to bring the separation point to the SJA. The actuation frequency ω_a is chosen as 60% of the shedding frequency for each angle for consistency, estimated from a previous study in a similar regime that was run at the same Re of 140,000 but at a slightly faster 20m/s from

(Golubev et al., 2015). The respective non-dimensional frequencies chosen are calculated and shown in Table 4.1. The full list of cases is shown in Table 4.2.

Table 4.1. Actuation Frequencies For NACA Cases Chosen From 60% Shedding.

AoA	Predicted Freq. (Hz)	Non-dimensionalized ω_a	~60% ω_a
0°	900	42.41147	24
2°	922	43.44819	26
4°	524	24.6929	15
8°	343	16.16348	10

Table 4.2. NACA Airfoil Test Case Descriptions.

Case Type	Case Name
Unaltered NACA Airfoil At AoA=0°	0° Clean
NACA Airfoil With Non-actuating Cavity At AoA=0°	0° Cavity
NACA Airfoil With Actuating Cavity At AoA=0°	0° Actuation
NACA Airfoil With Non-actuating Cavity At AoA=2°	2° Cavity
NACA Airfoil With Actuating Cavity At AoA=2°	2° Actuation
NACA Airfoil With Non-actuating Cavity At AoA=4°	4° Cavity
NACA Airfoil With Actuating Cavity At AoA=4°	4° Actuation
NACA Airfoil With Non-actuating Cavity At AoA=8°	8° Cavity
NACA Airfoil With Actuating Cavity At AoA=8°	8° Actuation

4.1. Actuation Effects on the Flow Field

If we examine the average *z*-vorticity in Figure 4.1, it is immediately apparent that this regime is very different than that of the high speed, low-Re transitional Joukowski airfoil simulations. *z*-vorticity represents the spin of the flow and is used to easily show the existence of vortices, as well as approximating the thickness of the boundary layer. For the low speed, high-Re transitional NACA simulations, a thinner boundary layer is observed, measuring at 3% chord for 0°AoA up to 6% chord at 8°AoA. The large recirculation zones previously seen in the Joukowski cases are also not seen, and while eddy formation does occur further up the chord from the trailing edge as AoA increases, the flow appears to stay mostly attached for the entire chord length except at

8°AoA where the eddies quickly detach from the surface. The point of separation will be further detailed in the next section.

Looking at the instantaneous vorticity contours at τ=81 in Figure 4.2 it is seen that actuation is enhancing the vortex bubble formation in this regime. This is further clarified in Figure 4.3 which zooms in at the SJA location. We see that the boundary layer thickness is half of what was seen in the Joukowski high speed regime. In this case, too much energy is being injected into the system. Instead of interrupting the vortex formation, the SJA is producing its own eddies.

Further study into this topic should vary the injection speed, governed by the SJA amplitude v_m. In this set of cases, v_m is kept at 0.5 to match with the v_m used for the Joukowski cases, which correlates to half of the upstream velocity. It is possible that a normalization factor for v_m in relation to the change in Re could be needed in order to find a v_m that does not overpower the vortex generation mechanism in this thinner boundary layer. There is also a possibility that without the presence of the separation/recirculation zone, it may not be possible to use SJAs in this regime for noise suppression.

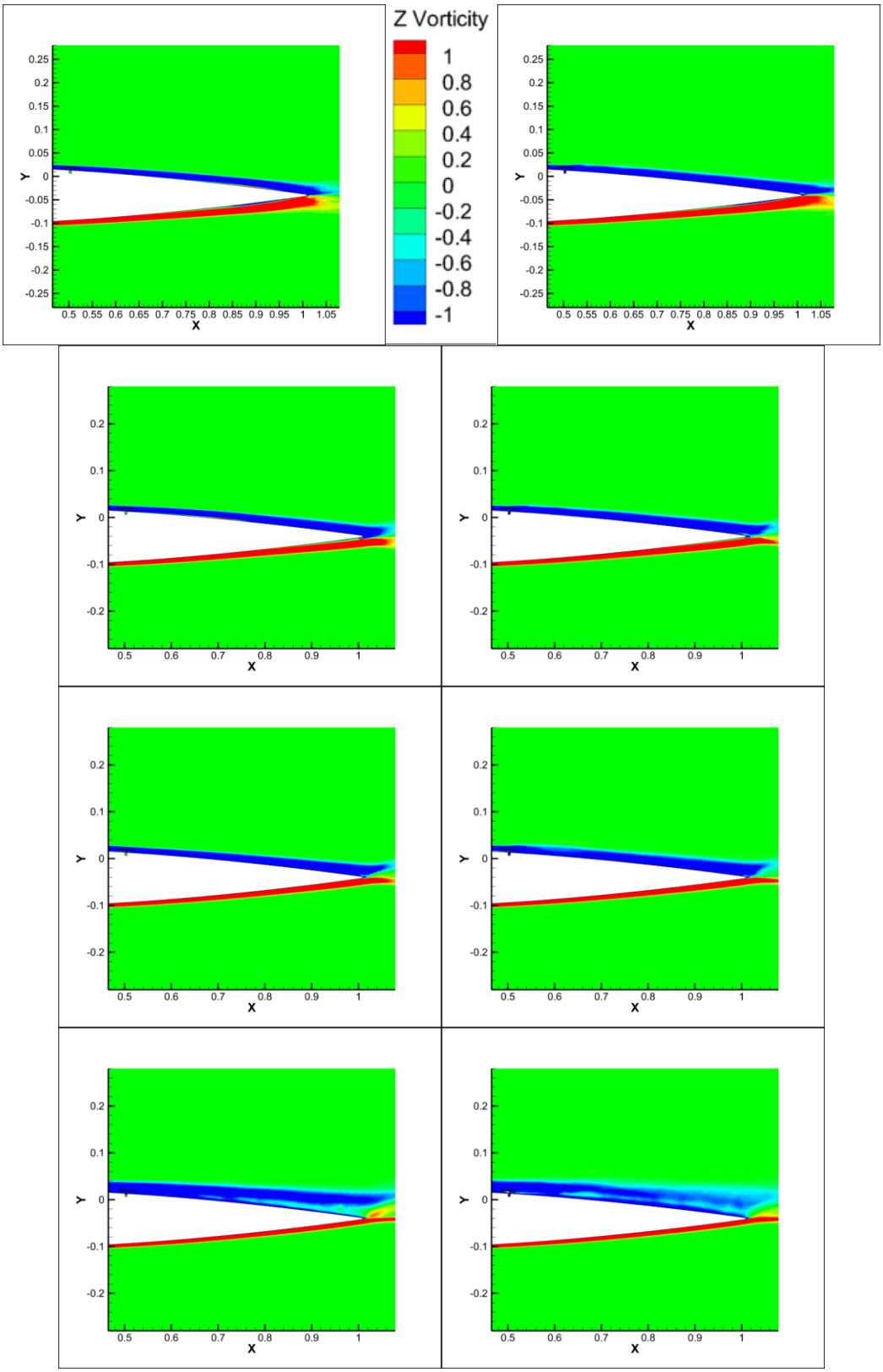

Figure 4.1. Average *z*-Vorticity Contours.
Cavity Cases (Left), Actuating Cases (Right).
0°AoA (First Row), 2°AoA (Second Row), 4°AoA (Third Row), 8°AoA (Fourth Row).

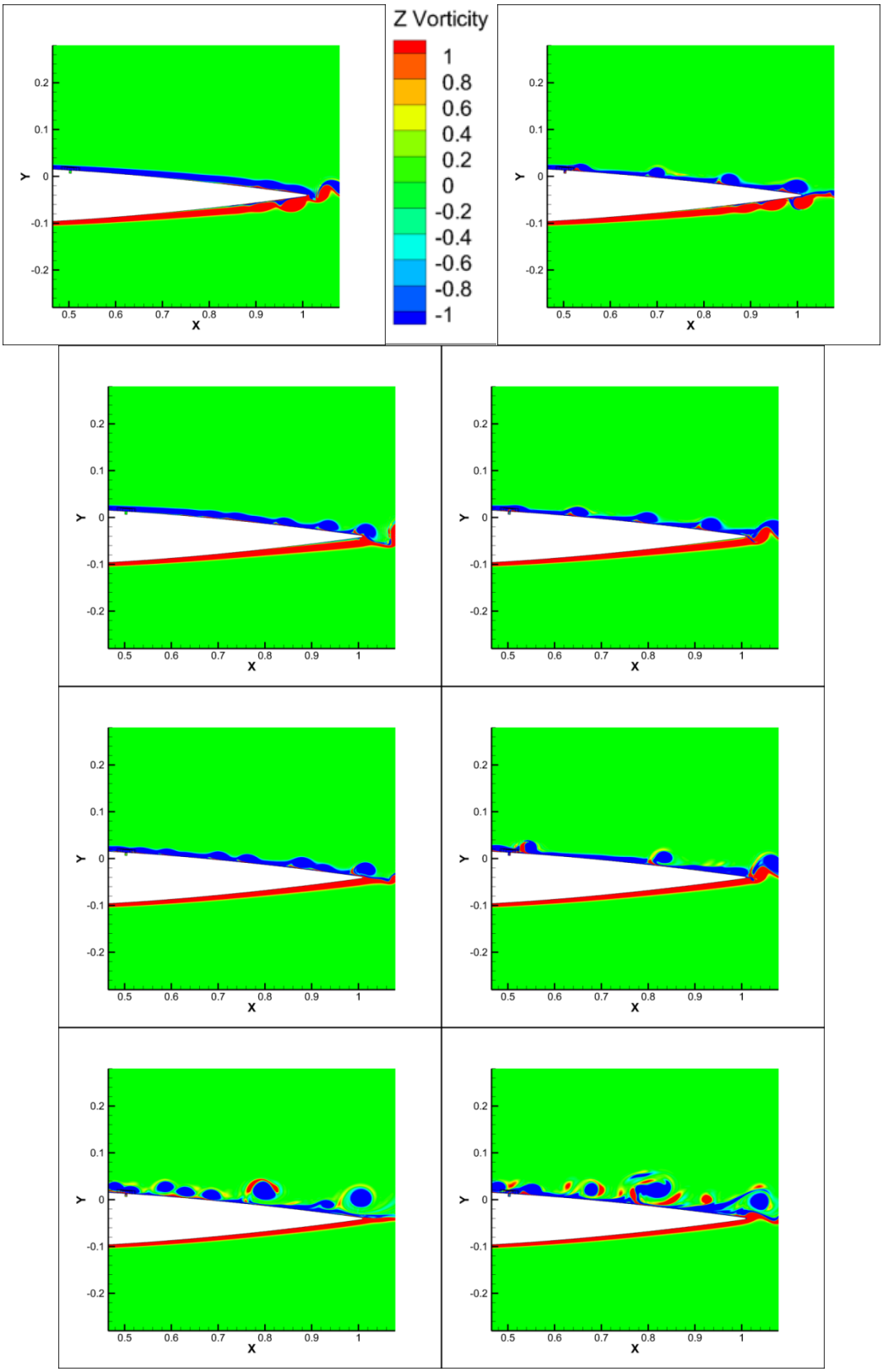

Figure 4.2. Instantaneous *z*-Vorticity Contours At $\tau=81$.
Cavity Cases (Left), Actuating Cases (Right).
0°AoA (First Row), 2°AoA (Second Row), 4°AoA (Third Row), 8°AoA (Fourth Row).

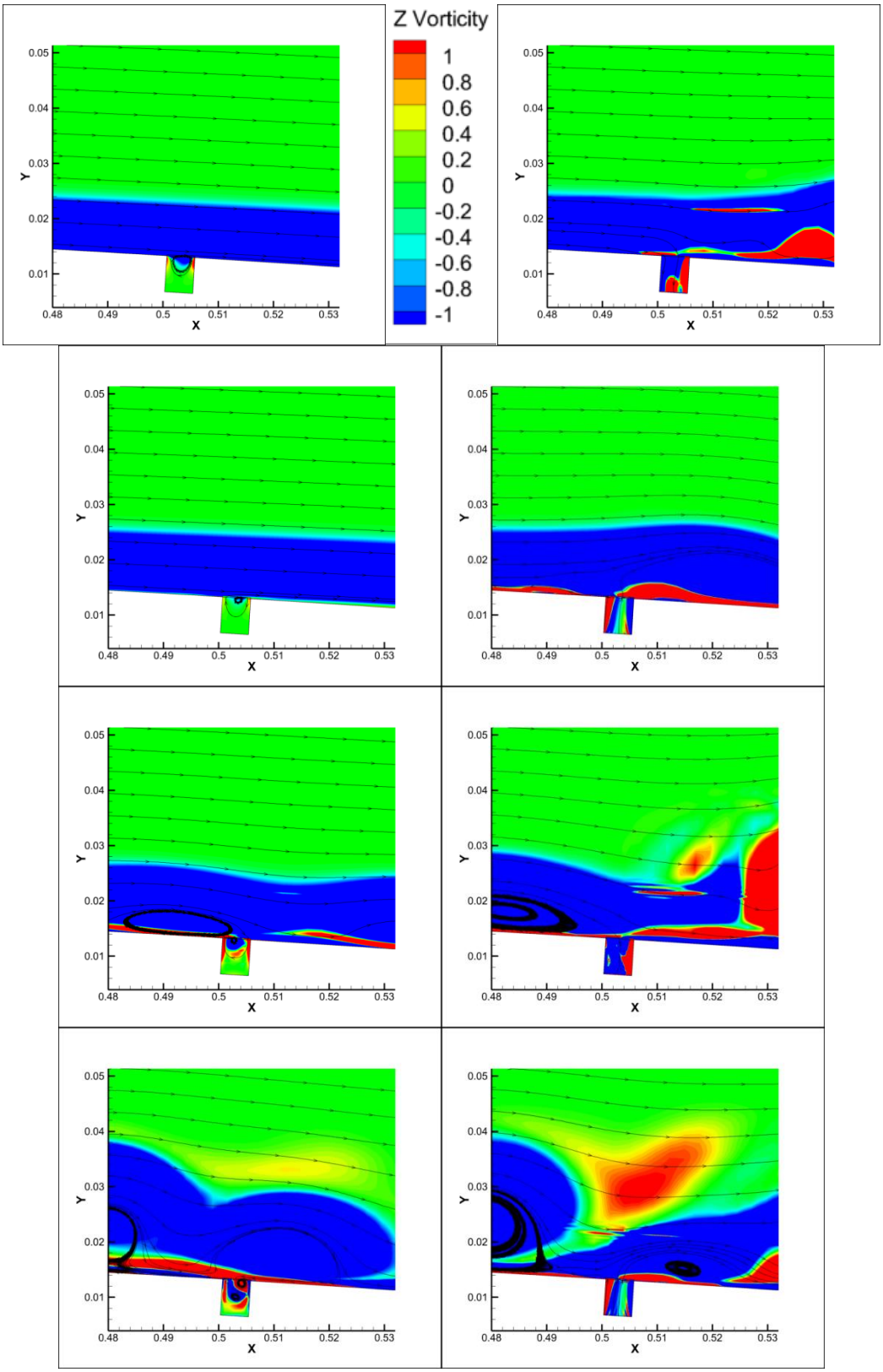

Figure 4.3. Instantaneous *z*-Vorticity Contours At SJA Region At $\tau=81$.
Cavity Cases (Left), Actuating Cases (Right).
0°AoA (First Row), 2°AoA (Second Row), 4°AoA (Third Row), 8°AoA (Fourth Row).

4.2. Actuation Effects on the Surface

Focusing on comparisons of surface pressure in Figure 4.4 we see once again that the geometry change caused by the introduction of the non-actuating SJA cavity has little effect on the flow for the 0°AoA case. The mean pressure shows no change other than a spike at the SJA location when actuation is turned on. With actuation turned on, there is almost no change in mean pressure when compared to the corresponding cavity cases for every AoA. However, for 4° and 8°AoA a spike similar to that seen from actuation cases is present, likely due to the interaction of the stagnation bubble inside the cavity with the rapidly shedding vortex eddies. Some deviation is seen after the characteristic spike at the SJA location on the top surface, but this area of deviation shrinks as the AoA increases, indicating that the SJA has less influence on the flow as the AoA increases. This is reinforced when looking at the P_{RMS}, where it is much clearer that the deviation between the non-actuating and actuating cavity flows decrease at the higher AoAs.

Looking at the lift response in Figure 4.5, we see that for this regime there is no increase in performance when the SJA is actuating for any AoA. Exact averages are given in Table 4.3. This was expected for the 0° and 2° cases as their separation point was predicted to not reach the midchord. In addition, the 4° and 8° cases are also unaffected and show little change. The 2° case has the only significant change with the lift history becoming more stable, similar to the change seen in the Joukowski cases, but increasing in amplitude.

Looking at the surface friction in Figure 4.6, it is shown for the 0° case that separation does not occur until 70% chord for the clean. As predicted this point is near the trailing edge. The cavity case is identical except for the local spike at the orifice

location, and some minor deviation at the trailing edge. With actuation, the separation point moves to the location of the SJA up the chord, with friction becoming negative in quick bursts before and after the orifice. The flow then reattaches and does not separate again. The SJA energizes the flow in a way that mimics separating the flow, inducing the formation of eddies earlier than in the non-actuating cases. The higher angle cases were investigated to determine if bringing the initial separation point to the SJA location at midchord would recreate the results seen in the Joukowski cases. However, even though the initial separation point does indeed travel up the chord as the AoA increases as depicted in Table 4.4, the effect the SJA has on the flow appears to diminish. In the highest angle case at 8°, the separation point is nearly at the leading edge, measuring at only 3% chord. With Actuation the surface friction is nearly identical, showing no significant impact on the flow.

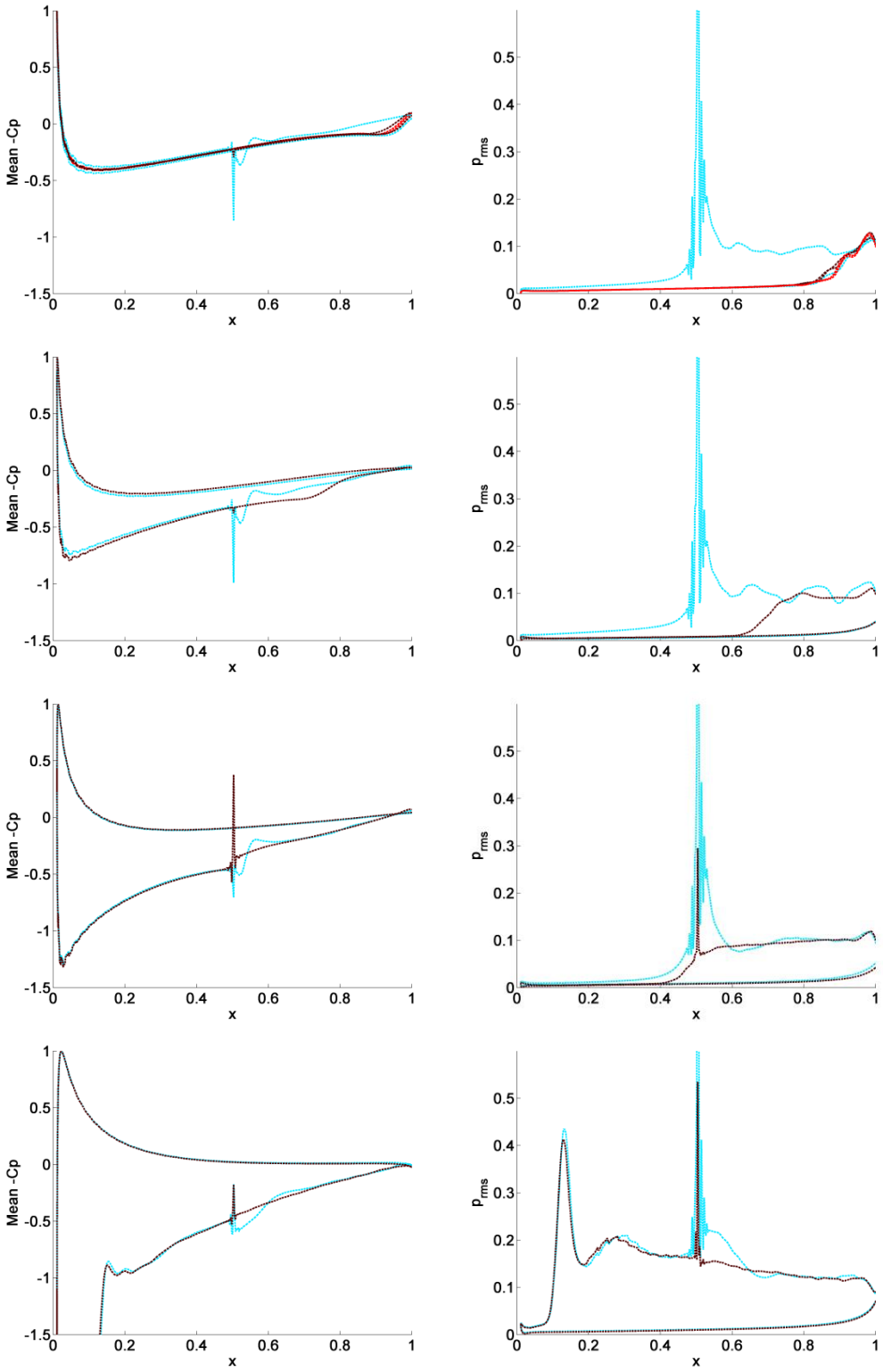

Figure 4.4. Pressure On Surface For NACA Cases.
Mean $-Cp$ (left) and P_{RMS} (Right).
Clean (Red), No Actuation Cavity (Black), Actuating Cavity (Cyan).
0°AoA (First Row), 2°AoA (Second Row), 4°AoA (Third Row), 8°AoA (Fourth Row).

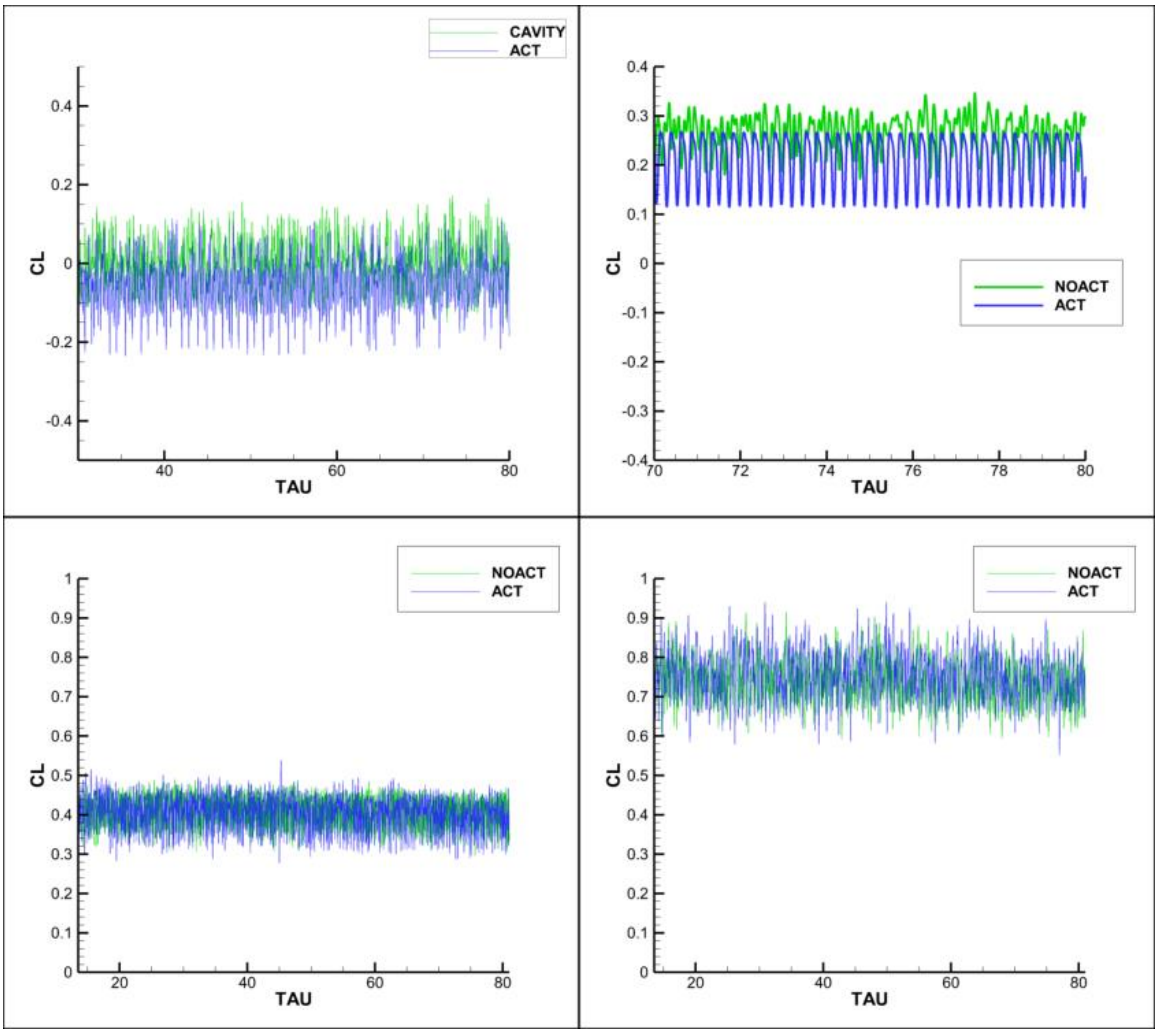

Figure 4.5. Lift History For All NACA Cases At Varying AoA.
Comparison Between No Actuation And Actuation At 60% Of Shedding Frequency.
4a: 0°AoA (Top-Left), 4b: 2°AoA (Top-Right) 4c: 4°AoA (Bottom-Left), 4d: 8°AoA.
(Bottom-Right) No Actuation Cavity (Green), Actuating Cavity (Blue).

Table 4.3. Average Lift For All NACA Cases.

AoA	**No Actuation**	**Actuation**
0	0.0025CL	-0.053CL
2	0.26CL	0.22CL
4	0.41CL	0.41CL
8	0.75CL	0.76CL

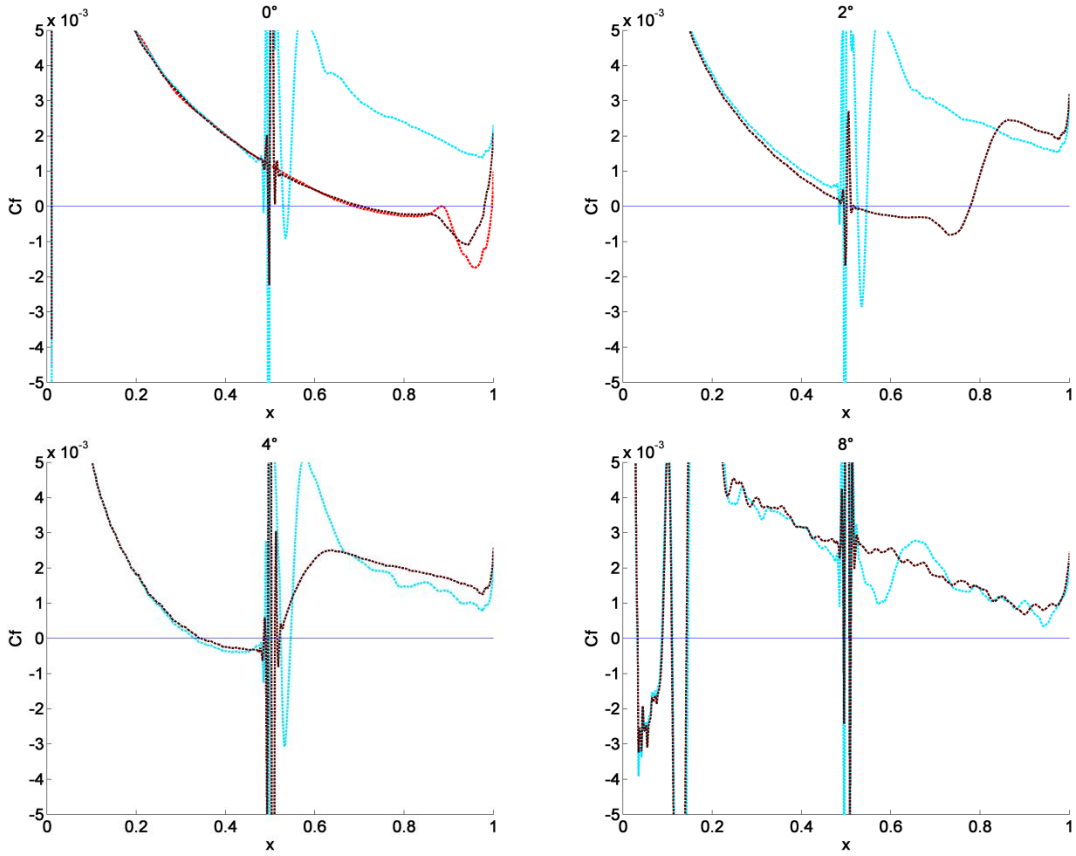

Figure 4.6. Surface Friction Along The Chord For Each Angle.
Clean (Red), No Actuation Cavity (Black), Actuating Cavity (Cyan).
0°AoA (Top Left), 2°AoA (Top Right), 4°AoA (Bottom Left), 8°AoA (Bottom Right).

Table 4.4. Initial Separation Point Location For NACA Cases.

AoA	No Actuation	Actuation
0	70% Chord	48% Chord
2	51% Chord	48% Chord
4	35% Chord	35% Chord
8	3% Chord	3% Chord

4.3. Actuation Effects on Noise

Similar to what was observed for the change in lift, we see that for the NACA cases actuating the SJA did not have a benefit, and in fact increased noise seen in the nearfield as shown in Figure 4.7. There is still little change between the clean case and

non-actuating cavity, so the clean case is neglected for the non-zero angle cases. The 2° case stands out once again as having the most generated noise, indicating that the SJA is overpowering the shedding vortex generation process and has become the dominant noise generator for that case.

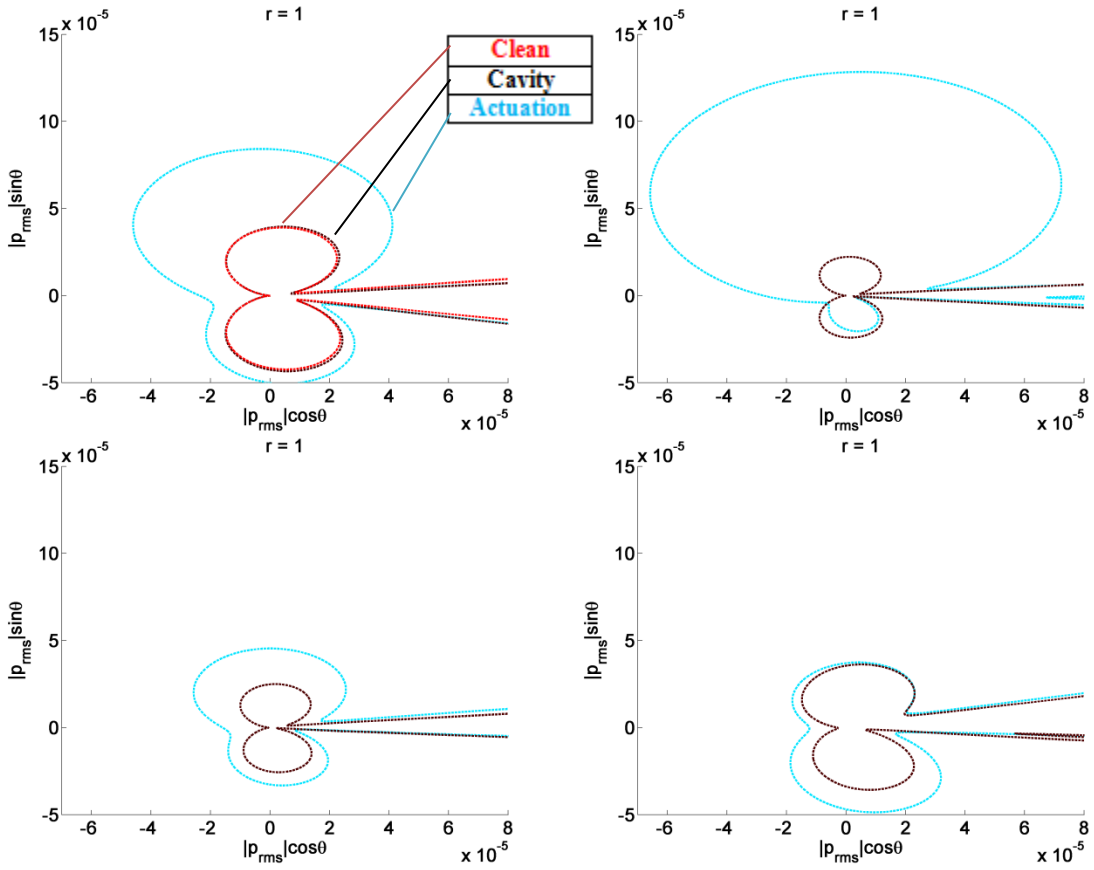

Figure 4.7. Acoustic P_{rms} Directivities At Radius 1c From Chord For NACA Cases. Clean (Red), No Actuation Cavity (Black), Actuating Cavity (Cyan). Top Left: 0°AoA, Top Right: 2°AoA, Bottom Left: 4°AoA, Bottom Right: 8°AoA.

The noise levels approach the base level for higher angles, which could indicate that boundary layer thickness at the SJA must be considered when choosing actuation parameters. The amplitude may be too high for this high-Re flow. The strength of this being an active control method is that in cases such as this, it is possible to simply turn off the actuator and have no negative effects. These results are also seen in the spectrum

analysis of each case. The P_{fft} harmonics are calculated using Matlab (R2014b) with a discrete Fourier transform command on pressure time histories. No windowing is used due to the limited sample size. Figure 4.8 shows the spectra 1 chord above midchord for each AoA. Once again, the 2° case stands out, this time with a broadband that is uncharacteristically thin. This is due to the nearly perfect periodic lift that was shown in Figure 3.10a. High tones are produced in each case, corresponding with the increase in noise shown in Figure 4.7.

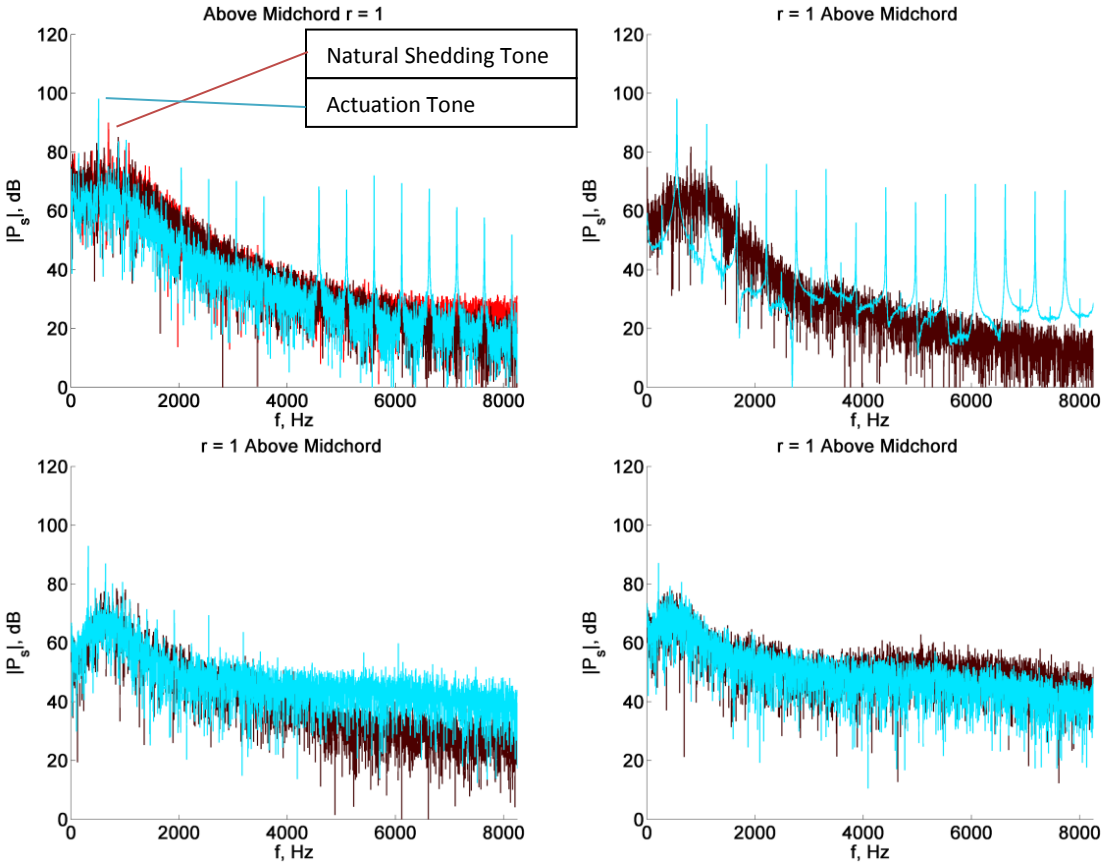

Figure 4.8. Acoustic Spectrum At Radius 1c Above Midchord. $dB\ Vs\ f$.
Clean (Red), No Actuation Cavity (Black), Actuating Cavity (Cyan).
Top Left: 0°Aoa, Top Right: 2°AoA, Bottom Left: 4°AoA, Bottom Right: 8°AoA.

5. Conclusion

This work implemented a high-accuracy numerical analysis to examine effect of synthetic-jet actuation on sound radiated by transitional, symmetric, 12%-thick Joukowski airfoil at M=0.5, Re=50,000 and NACA 0012 at M=0.0465, Re=140,000 in uniform upstream flows.

The Joukowski airfoil cases were characterized by large separation zones that developed into large vortical structures scattering into acoustic waves at the trailing edge. The switching of the separation bubble was suggested as the primary mechanism of the tonal trailing-edge noise in the absence of impinging flow disturbances.

For the baseline case of the actuator located at the midchord position near the laminar separation point, we showed in our previous study (Mankbadi, 2014) that the addition of a SJA could dampen the noise generation in this regime. This is consistent with our current results which have been improved with higher sampling. The actuated SJA injects energy into the thick boundary layer, which disrupts the recirculation zone and interferes with the vortex generation process.

The data from the previous study (Mankbadi, 2014) showed a peak tone appears at the natural shedding frequency of 10.47. The addition of the non-actuating cavity amplified the tone, but when actuation was turned on this tone disappeared, and a new peak tone appeared at the actuation frequency, along with higher harmonics. In the current study, the primary shedding tone is successfully dampened again, and the strength of the new tone corresponding with actuation frequency is lower than that of the baseline tone for all frequencies except for $\omega_a = 21$ which was shown to have minimal noise reduction. The primary result of the dampening of the shedding tone holds true when

compared to the earlier data, however the increased sampling shows that the cavity tone and higher harmonics are not as prevalent. This is also due to a scaling error that was resolved since the initial findings.

The Joukowski airfoil in the high speed, low-Re regime exhibited a periodic lift pattern associated with the unstable laminar separation region that forms at the trailing edge and periodically switches its primary position between the airfoil upper and lower surfaces. Comparison of the previous data shows similar levels for the lift on the clean and cavity cases. With the uniform upstream flow condition, the actuated cavity produced a regularizing effect on the airfoil lift response associated with continuously energized boundary layer on the upper surface. This is seen in both the earlier study and the current data.

The position of separation was measured to be at 40% chord for the clean Joukowski airfoil. With the addition of SJA actuation, separation was delayed to 45% chord. This ability to control/delay the separation point could potentially be used as a method of increasing $C_{L\,max}$, and is one of many directions this study could be built upon with future work.

Next, the effects of the actuation frequency on the trailing-edge noise radiation were tested, with results showing suppression of the noise for all frequencies considered (including shedding frequency). A trend emerged that suggested local maximums exist for noise reduction at frequencies surrounding the natural shedding frequency. This change in P_{rms} levels revealed a trend that was comparable to the average lift gains, suggesting that there is a correlation between suppression of tones and lift.

Positioning the SJA near the trailing edge revealed almost no effect on the

trailing-edge noise suppression compared to the non-actuating case. It was concluded that the SJA must be positioned somewhere upstream in order for its effects to propagate. Further studies could investigate more locations, but the current location set at the midchord separation point has already shown to be a viable position.

For the NACA 0012 airfoil in the low speed, high-Re regime, SJA actuation had negative effects for all angles of attack. Noise generation was increased and higher tones were produced due to the extra energy added to the flow that failed to dampen the transitional switching of the separation bubble.

Unlike the low-Re Joukowski airfoil cases, the high-Re NACA airfoil cases have a much thinner boundary layer. Possibly due to this thinner boundary layer, the flow was overpowered by the SJA, and more separation bubbles were produced, amplifying the vortex shedding at the trailing edge, which in turn produced more noise. In further studies, smaller amplitudes should be tested. This would take into account the high-Re of the regime when compared to the low-Re of the Joukowski regime which did successfully show noise suppression.

Another major difference seen is that unlike the Joukowski airfoil cases, the NACA airfoil cases have no recirculation region. As this region was heavily affected by the actuation in the Joukowski regime, its absence in the NACA regime is another likely reason the noise was increased and not dampened.

The results of this study indicate that it is possible to suppress trailing edge noise by using a SJA. However, the possible benefits of the SJA are dependent on the flow characteristics of the airfoil. Under certain conditions, SJA actuation will interfere with the transitional switching of the separation bubbles of the regime and dampen the existing

tones. If these currently unknown conditions are not met, the SJA will add more energy to the flow, resulting in higher noise levels. The existence of one regime in which SJA noise suppression is possible gives the possibility of more such regimes and warrants further investigations.

6. Recommendations

The most difficult challenges of this study were related to ever evolving procedures and their scripting. At this point, much of the required procedures have been streamlined for future use through various scripts. It is recommended that if this study is continued that the new researcher make use of these scripts to cut down on post-processing time. There are still many paths that are unexplored by this study that warrant future research. Along with the search for additional regimes in which the SJA noise suppression is possible, the SJA parameters themselves still require more testing. A proper scaling method for v_m that takes Re into consideration is necessary to fully complete this research. A larger range of frequencies and SJA locations can also be investigated for further optimization of SJA use.

7. REFERENCES

Arbey, H., & Bataille, J. (1983). Noise generated by airfoil profiles placed in a uniform laminar flow. Journal of Fluid Mechanics, Vol. 134, pp. 33-47.

Callicoat, J., Arena, A., Gaeta, R., & Jacob J. (2013). Design Considerations for Developing Composite Materials Providing Improved Acoustic Transmission Loss for UAVs. AIAA Paper 2013-0465, 51st AIAA Aerospace Sciences Meeting including the New Horizons Forum and Aerospace Exposition, Grapevine, TX, January.

Desquesnes, G., Terracol, M., and Sagaut, P. (2007). Numerical investigations of the tone noise mechanism over laminar airfoils. Journal of Fluid Mechanics, Vol. 591, pp. 155.

Ewert, R. & Manoha, E. (2007). Trailing-Edge Noise. In: Wagner, C., Huttle, T. and Sagaut, P. Large-Eddy Simulation for Acoustics. Cambridge University Press, pp. 293-333.

Gaitonde, D.V., & Visbal, M.R. (1998). High-Order Schemes for Navier–Stokes Equations: Algorithm and Implementation into FDL3DI. Air Force Research Laboratory Tech. Rep. TR-1998-3060, Wright-Patterson Air Force Base, OH.

Glezer, Ari, & Michael Amitay, (2002). Synthetic jets. Annual Review of Fluid Mechanics, Vol. 34.1, pp. 503-529.

Golubev, V.V., Nguyen, L. & Visbal, M.R. (2010). High-Fidelity Viscous Simulations of Airfoil Noise Radiation in Nonuniform Unsteady Flow. AIAA 2010-3761, 16th AIAA/CEAS Aeroacoustics Conference, Stockholm, Sweden, June.

Golubev, V.V., Nguyen, L., & Visbal, M.R. (2010). High-Accuracy Low-Re Simulations of Airfoil-Gust and Airfoil-Vortex Interactions. AIAA Paper 2010-4868, 40th Fluid Dynamics Conference and Exhibit, Chicago, IL, June.

Golubev, V.V., Nguyen, L., Roger, M., & Visbal, M.R. (2011). On Interaction of Airfoil Leading and Trailing Edge Noise Sources in Turbulent Flow. AIAA Paper 2011-2859, 17th AIAA/CEAS Aeroacoustics Conference, Portland, OR, June.

Golubev, V.V., & Visbal, M.R. (2012). Modeling MAV Response in Gusty Urban Environment. International Journal of Micro Air Vehicles, Vol.4, pp. 79-92.

Golubev, V.V., Nguyen, L., Mankbadi, R.R., Roger, M. & Visbal, M.R. (2014). On Flow-Acoustic Resonant Interactions in Transitional Airfoils. International Journal of Aeroacoustics, Vol. 13, pp. 1-38.

Golubev, V. V, Sansone, M. & Nguyen, L. & Mankbadi, R., R. (2015). Numerical Study of Synthetic-Jet Actuation Effect on Leading and Trailing Edge Noise. AIAA Paper 2015-0010, 53rd AIAA Aerospace Sciences Meeting, Kissimmee, FL, January.

Golubev, V.V., Nguyen, L., Hiner, W., Sansone, M., Salehian, S. & Mankbadi, R. (2015). Parametric Investigations of Tonal Trailing-Edge Noise Generation by Moderate Reynolds Number Airfoils Part II – Numerical Studies. AIAA Paper 2015-2528, 21st AIAA/CEAS Aeroacoustics Conference, Dallas, TX, June.

Mankbadi, R., R., Golubev, V. V, Sansone, M., Sewell, C. & Nguyen, L. (2014). Effect of A Synthetic Jet Actuator on Airfoil Trailing-Edge Noise. International Journal of Aeroacoustics, Vol. 14, pp. 553 – 568.

Nash, E. C., Lowson, M. V., & McAlpine, A. (1999). Boundary-layer instability noise on aerofoils. Journal of Fluid Mechanics, Vol. 382, pp. 27-61.

Patterson, R., Vogt, P., Fink, M., & Munch, C. (1973). Vortex noise of isolated airfoils. Journal of Aircraft, Vol. 36, pp. 296-302.

Raju, R., Aram, E., Mittal, R. & Cattafesta, L. (2009). Simple Models of Zero-Net Mass-Flux Jets for Flow Control Simulations. International Journal of Flow Control, Vol. 1, pp. 179-197.

Rizzetta, D. P., Visbal, M.R., & Stanek, M.J. (1999). Numerical Investigation of Synthetic-Jet Flowfields. AIAA J., Vol. 37, pp. 919-927.

Scott, J.R. (2004). Single Airfoil Gust Response Problem. Proceedings of the 4th CAA Workshop on Benchmark Problems, NASA CP-2004-212954, pp.45-48.

Sewell, Cody B. (2012). Reduction of the Acoustic Emissions of an Airfoil in an Impinging Gust. M.S. Thesis, Aerospace Engineering Dept., Embry-Riddle Aeronautical University, Daytona Beach, FL.

Sherer, S.E., Visbal, M.R. & Galbraith, M.C. (2006). Automated Preprocessing Tools for Use with a High-Order Overset-Grid Algorithm. AIAA Paper 2006-1147, 44th AIAA Aerospace Sciences Meeting and Exhibit, Reno, NV, January.

Suhs, N.E., Rogers, S.E. & Dietz, W.E. (2002). PEGASUS 5: An Automated Pre-processor for Overset-Grid CFD. AIAA Paper 2002-3186, 32nd AIAA Fluid Dynamics Conference and Exhibit, Louis, MO, June.

Tam, C. K. (1974). Discrete tones of isolated airfoils. Journal of the Acoustical Society of America, Vol. 55 (no. 6, June), pp. 1173-1177.

Visbal, M.R. & Gaitonde, D.V. (2002). On the Use of High-Order Finite-Difference Schemes on Curvilinear and Deforming Meshes. Journal of Computational Physics, Vol. 181, pp.155–185.

Visbal, M.R., Morgan, P.E. & Rizzetta, D.P. (2003). An Implicit LES Approach Based on High-Order Compact Differencing and Filtering Schemes. AIAA Paper 2003-4098, 16th AIAA Computational Fluid Dynamics Conference, Orlando, FL, June.